1 **Gravity Effect of Alpine Slab Segments Based on Geophysical and Petrological Modelling**

2 Maximilian Lowe [1,2,3], Jörg Ebbing [1], Amr El-Sharkawy [1,4], Thomas Meier [1]
3
4 [1] Institute for Geosciences, Kiel University, Germany
5 [2] NERC British Antarctic Survey, Cambridge, United Kingdom
6 [3] School of geosciences, University of Edinburgh, United Kingdom
7 [4] National Research Institute of Astronomy and Geophysics (NRIAG), 11421, Helwan, Cairo, Egypt
8
9 Correspondence to Maximilian Lowe: maxwe32@bas.ac.uk

11 **Abstract**

12 In this study, we present an estimate of the gravity signal of the slabs beneath the Alpine
13 mountain belt. Estimates of the gravity effect of the subducting slabs are often omitted or
14 simplified in crustal scale models. The related signal is here calculated for alternative slab
15 configurations at near surface height and on a satellite altitude of 225 km.
16 We apply three different modelling approaches in order to estimate the gravity signal from the
17 subducting slab segments, by: i) Direct conversion of upper mantle seismic velocities to density
18 distribution, which are then forward calculated to obtain the gravity signal. ii) Definition of slab
19 geometries based on seismic crustal thickness and high-resolution upper mantle tomography
20 for two competing slab configurations. The geometries are then forward calculated by assigning
21 a constant density contrast and slab thickness. iii) Accounting for compositional and thermal
22 variations with depth within the predefined slab geometry.
23 Forward calculations predict a gravity signal of up to 40 mGal for the Alpine slab configuration.
24 Significant differences in the gravity anomaly patterns are visible for different slab geometries
25 in the near surface gravity field. However, different contributing slab segments are not easily
26 separated, especially at satellite altitude. Our results demonstrate that future studies addressing
27 the lithospheric structure of the Alps should have to account for the subducting slabs in order
28 to provide a meaningful representation of the geodynamic complex Alpine area.
29
30 Keywords:
31 Satellite gravity gradient, Alpine subduction, lithospheric and sub lithospheric structure, mantle
32 composition, seismic tomography

34 **1. Introduction**

35 Interpretation of gravity anomalies can reveal information on the architecture and tectonic

36 setting of the lithosphere (e.g. Zeyen, & Fernàndez, 1994; McKenzie & Fairhead, 1997;

37 Holzrichter & Ebbing, 2006; Braitenberg, 2015; Spooner et al. 2019). For subduction zones,

38 like the Andes, several studies have shown that the gravity effect of the subducting plates is

39 significant and has to be considered in order to study the feedback between the subducting

40 lithosphere and the overriding plate (Götze et al. 1994; Götze & Krause 2002; Tašárová 2007

41 Gutknecht et al. 2014; Götze & Pail 2018; Mahatsente 2019). For lithosphere to subduct, a

42 higher density than the surrounding mantle material at the same depth interval is required,

43 causing a negative buoyancy for the slab and therefore the slab is subducted into earth's interior

44 (e.g. Kincaid & Olson 1987; Ganguly et al. 2009). However, the gravitational contribution of

45 subducting material in the upper mantle to the gravity field has so far not been systematically

46 addressed for the Alpine system. In order to provide an assessment, the magnitude of the gravity

47 signal of such sub-crustal long wavelength features has to be estimated.

48 The Alpine mountain belt (Fig. 1a) is chosen for this sensitivity study because firstly a large

49 range of recent seismic tomography studies imaged subducting slab segments in the Alpine

50 region (e.g. Babuska et al., 1990; Lippitsch et al., 2003; Spakman & Wortel, 2004; Mitterbauer

51 et al. 2011; Karousová et al., 2013; Zhao et al., 2016; Kästle et al., 2018; El-Sharkawy et al.,

52 2020). Those different studies suggest different configurations of slab segments (see section

53 1.1), allowing us to test how sensitive the gravity field is to varying geometries of subducting

54 slab segments. Secondly, previous Alpine models addressing the Alpine gravity field have

55 considered the subcrustal mantle inhomogeneities in form of lithosphere thickness (e.g. Ebbing

56 et al., 2006; Spooner et al., 2019) or in form of mantle density variations (Tadiello and

57 Braitenberg 2021), but without identifying the isolated effect of subducting slabs segments in

58 the velocity or density variations. If the contribution of the mantle density variations is not

59 considered, a significant part of the gravity field might be attributed to crustal thickness

60 variations or intra-crustal sources.

61 In addition, the Bouguer Anomaly of the Alps (Fig. 1b) shows no direct sign of subducting slabs

62 (in contrast to the Andes subduct zone) as the field is dominated by crustal thickness variations

63 (Ebbing et al., 2001, 2006). Therefore, forward modeling of the proposed slab geometries, as

64 imaged by high-resolution tomographic studies, is neecesary to separate the gravity signal

65 caused by the suducting slabs from the gravity anomnaly field.
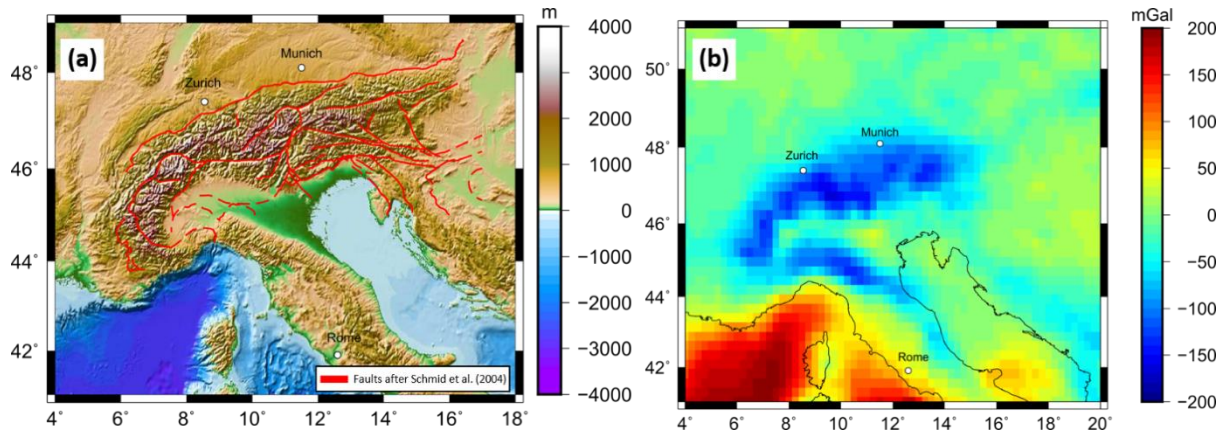
66

67 *Figure 1 **(a)** Topography from ETOPO1 from Amante and Eakins (2009). Faults in red after Schmid et al. (2004). **(b)** Bouguer*
68 *Anomaly based on XGM 2019 (Zingerle et al., 2020) with a maximum spherical harmonics degree of 719 at a station height of*
69 *6040m above the ellipsoid, just above the surface of the Alps. Correction density for rock: 2670 kg/m³ and for water: 1030*
70 *kg/m³*

71 We present three different approaches to model the gravity effect of the slab segments and

72 discuss the strengths and limitations of the applied methods. In the first approach, the alpine

73 sup-crustal density distribution is derived by converting seismic velocities to density. This

74 model is then forward calculated to estimate the gravity response. In the second approach, 3D

75 slab geometries are derived by evaluating seismic crustal thickness estimations and high-

76 resolution upper mantle tomographic models. Here, two competing slab configurations are

77 chosen. The predefined slab geometries are then forward calculated by assigning different

78 density contrasts and slab thicknesses. The third approach uses similar predefined slab

79 configurations as in the second approach, however, here we consider petrology, temperature,

80 and density variation. The gravity response is calculated for all three approaches at a near

81 surface height for the gravity disturbance and the gravity gradients at satellite altitude of 225

82 km.

83 1.1 Alpine setting
84 The formation and present geodynamics of the Alps are linked to long lasting tectonic

85 processes, including Adria-Europe continent-continent collision, subduction of oceanic and

86 continental lithosphere, the formation of crustal nappes as well as extensional and

87 ~~compressional~~ shortening processes (Frisch, 1979; Stampfli & Borel, 2002; Handy, et al., 2010,

88 2015). The Adriatic microplate is a major driver of the present geodynamics in the Alpine

89 region, which is trapped between the converging major plates of Europe and Africa. Adria is

90 moving counterclockwise with respect to Europe, as seen by GPS observations (e.g. Nocquet

91 and Calais, 2004; Vrabec and Fodor, 2006; Serpelloni et al., 2016) and is subducted beneath the

92 Apennines to the west as well as to the east beneath the Dinarides, while colliding with Eurasia

93 in the Alps to the north (e.g. Channel & Horvath, 1976; Dewey et al., 1989; Stampfli & Borel,

94 2002; Handy et al., 2010; Le Breton et al., 2017). Subducting slab segments have been imaged

95 by different seismological body wave travel time tomographic studies as well as surface wave

96 tomographic studies within the Alpine upper mantle (e.g. Babuska et al., 1990; Lippitsch et al.,

97 2003; Spakman & Wortel, 2004; Mitterbauer et al. 2011; Karousová et al., 2013; Zhao et al.,

98 2016; Kästle et al., 2018; El-Sharkawy et al., 2020). However, the configuration of subducting

99 slab segments remains controversial. In the Western Alps, Lippitsch et al. (2003) propose a slab

100 break-off at about 100 km depth, which is in line with the findings of Beller et al. (2018), Kästle

101 et al. (2018) and El-Sharkawy et al. (2020). In contrast, a continuous subducting slab segment

102 in the Western Alps, down to at least 250 km depth, is imaged by a number of other tomographic

103 models (e.g. Koulakov et al., 2009; Zhao et al., 2016; Hua et al., 2017; Lyu et al., 2017).

104 A continuous subduction of Eurasia beneath the Central Alps down to at least 200 km depth is

105 imaged by different tomographic models (e.g. Lippitsch et al., 2003; Piromallo and Morelli,

106 2003; Koulakov et al., 2009; Mitterbauer et al., 2011; Hua et al., 2017; Fichtner et al., 2018; El-

107 Sharkawy et al., 2020). A potential slab gap with an approximate size of 2° is separating the

108 subducting slab segments in the Central Alps to the Eastern Alps as imaged by e.g. Lippitsch

109 et al. (2003). The slab configuration and subduction direction in the Eastern Alps remains

110 unclear. According to the classical view, Eurasia is subducting beneath Adria in a southward

111 subduction (Hawkesworth et al., 1975; Lüschen et al., 2004; 2006). This idea was challenged

112 by Lippitsch et al. (2003), Schmid et al. (2004), Kissling et al. (2006), Handy et al. (2015), and

113 Hetenyi et al. (2018). Instead, slab break-off in the eastern Alps and a northward-dipping

114 Adriatic slab in the easternmost Alps is suggested, leading to a switch of the slab polarity, as

115   Adria is subducting beneath the European plate (Handy et al., 2015). The view that Adriatic and

116   not Eurasian lithosphere is subducting northwards in the Eastern Alps has been opposed by

117   Mitterbauer et al. (2011), as their model shows a northward dipping slab in the eastern most

118   Alps connected to the European plate. In an early tomographic study, Babuska et al. (1990)

119   proposed that both Eurasian and Adriatic lithosphere is subducting in the eastern Alps. In

120   subsequent studies and interpretations this model was mentioned but northward subduction of

121   Adria seems to be favoured (e.g. Karousová et al., 2013; Hetenyi et al., 2018), Recently,

122   subduction of both Eurasian and Adriatic lithosphere in the eastern Alps down to about 150 km

123   has been suggested by Kästle et al. (2020) and El-Sharkawy et al. (2020) based on surface wave

124   studies. For a more in-depth comparison and discussion of tomographic Alpine models the

125   reader is referred to e.g. Kästle et al. (2020).

126   **2. Data**

127   The Bouguer Anomaly (Fig. 1b) is based on the global model *XGM 2019* (Zingerle et al., 2020)

128   developed for spherical harmonics up to degree 719, with a resolution of ~25 km (half

129   wavelength). The XGM 2019 model is a global integrated gravity model, which includes

130   satellite and terrestrial measurements. The Bouguer Anomaly is calculated from the Free-Air

131   gravity disturbance with a correction density of 2670 kg/m^3 for topography, and a correction

132   density for water of 1030 kg/m^3 for the offshore areas using Tesseroids (Uieda et al., 2016). For

133   the tesseroids, we use the topography and bathymetry from ETOPO (Amante & Eakins, 2009),

134   which was regridded at a regular grid with a grid space of 25 km to match the resolution of the

135   XGM 2019 model for a maximum degree of 719. The gravity field is defined at a constant

136   station height of 6040 m above the ellipsoid, just above the surface of the Alps. The resulting

137   Bouguer Anomaly shows a gravity low in the order of -200 mGal over the high topography of

138   the Alps, indicating an isostatic crustal thickening in response to topography (e.g. Ebbing et al.,

139   2006). Additionally, we calculate the mass correction for the gravity gradients at a station height

140 of 225 km representing the GOCE satellite altitude. The topographic corrected gravity gradients

141 after Bouman et al. (2016) measured by the GOCE ESA satellite mission are presented in the

142 appendix.

143 For the definition of the slab geometry, we use crustal thickness estimates based on the receiver

144 function study by Spada et al. (2013). The crustal thickness map was digitized and the Moho

145 gap in the eastern Alps is filled by nearest neighbour interpolation. To avoid edge effects,

146 surrounding areas are supplemented by the Moho depth model of the European plate by Grad

147 et al. (2009), both data sets were merged using a cosine taper with a taper width of 2° using

148 equation (1). The overlapping areas at the grid edges are distance weighted to obtain a smooth

149 transition.

150
$$G_{new} = T(x,y) \cdot G_1(x,y) + \big(1 - T(x,y)\big)G_2 \cdot (x,y)) \quad (1)$$

152
$$with: T(x,y) = cos\frac{D \cdot \pi}{2 \cdot L}$$

151
with: G = Grids, T = taper, D =dx, L = Tapper length

153 The merged Moho depth map is sampled at a regular grid with a cell size of 0.25° (Fig. 2) to be

154 consisted with resolution of the topographic and gravity models.

155
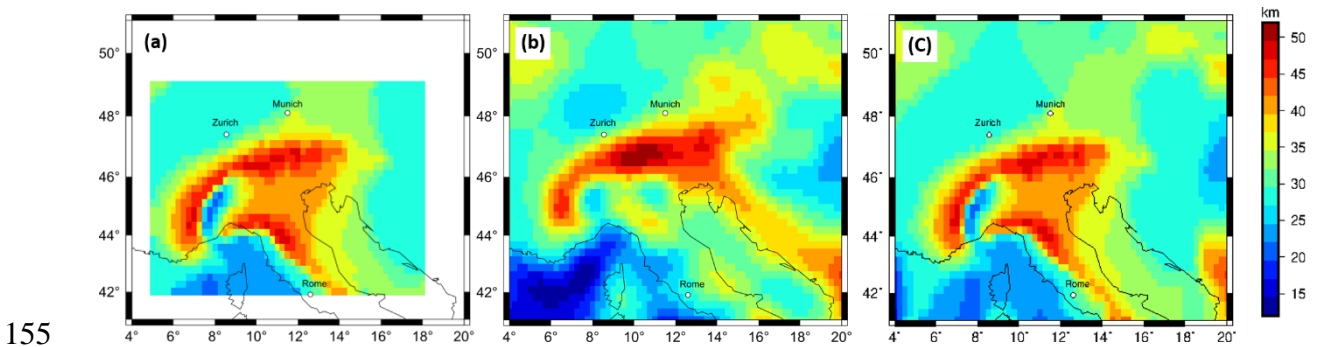
156 *Figure 2 a) digitized Moho depth after Spada et al. (2013) with a 0.25 ° grid spacing, b) Moho depth estimation after Grad et*
157 *al. (2009) with a 0.25 ° grid spacing c) Merged Moho depth map from Spada et al. (2016) and Grad et al. (2009) with a grid*
158 *resolution of 0.25 ° using a cosine taper with a 2° width.*

159 For the upper mantle seismic velocity, the 3-D shear wave velocity model (MeRE2020) by El-

160 Sharkawy et al., (2020) is used (Fig. 3). The model covers the upper mantle across the Alpine-

161 Mediterranean area down to a depth of 300 km and absolute shear-wave velocities are given.

162   In this study, relative shear-wave velocities in the depth range from 70 to 200 km are calculated

163   with respect to a 1-D average shear wave velocity model, the background model is described in

164   El-Sharkawy et al., (2020). The upper limit of 70 km is introduced because i) we focus on the

165   contribution of the slab segments removing therefore crustal information from the model ii) the

166   tomography model MeRE2020 is not sensitive to shallow structures, as a result the slabs are

167   not well recovered in depths shallower than 70 km iii) we want to ensure a uniform upper

168   boundary. The lower boundary of 200 km is chosen based on clear images of the Alpine Slab

169   segments to at least 200 km depth (with exception of the Western Alpine slab), as discussed in

170   section 1, and the assumptions that depth larger than 200 km will have a negligible effect on

171   the regional gravity field considered here.

172   The ambient noise tomography by Kästle et al. (2018) is used to define the geometry of the

173   Western Alpine slab segment, hence we follow the idea of a slab-breakoff in the Western Alps

174   at 100 km depth (Kästle et al., 2020) as suggested also by Lippitsch et al. (2003) and Beller et

175   al. (2018). For the eastern Alps, we consider two alternative models. For the first hypothesis,

176   the P-wave tomography by Lippitsch et al. (2003) is used, to define the Eastern Alpine slab

177   segment. The second hypothesis is based on Kästle et al. (2020) and El-Sharkawy et al. (2020).

178   It assumes southward subduction of a short Eurasian Slab as well as northward subduction of a

179   short Adriatic Slab in the eastern Alps. The slab configurations which are incorporated in the

180   Alpine density models are discussed in greater detail in section 4.1.

181   **3 Conversion of seismic velocities into density distribution**

182   Seismic velocity variations are dependent on temperature and pressure. Densities in the

183   subsurface are also temperature and pressure dependent. A conversion factor (ζ) can describe

184   the linear relation between seismic velocities variations and densities variation (e.g. Tiberi et al.

185   2001; Webb 2009). We convert seismic shear wave velocities from the tomographic model

186   MeRE2020 by El-Sharawy et al. (2020) in the depth range from 70 to 200 km, as discussed in

187   section 2, to obtain a density distribution of the upper mantle in the Alpine region based on a

188   conversion factor (ζ). The relationship between seismic velocities and densities is described in

189   equation (2), this assumption is a strong simplification of reality, but gives a first order

190   estimation of the expected relative density structure beneath the Alps.

191     $$\rho_{rel} = [Vsv_{abs}(1 + \Delta\%) - Vsv_{abs}] \cdot \zeta = Vsv_{abs} \cdot \Delta\% \cdot \zeta \quad (2)$$

192     $with: Vsv_{abs} = \ absolute\ velocities\ from\ MeRE2020;$

193     $\Delta\% = \ percentage\ deviation\ from\ the\ MeRE2020\ background\ model;$

194     $\zeta = \ conversion\ factor$

195   The result is strongly dependent on the chosen conversion factor. A range for conversion

196   factors has been proposed in the literature for different rock types ranging from 0.1 to 0.45 (e.g.

197   Isaac et al., 1989; Isaak, 1992; Karato, 1993; Kogan and McNutt, 1993; Vacher et al., 1998).

198   The relative shear-wave velocity distribution in a 3D domain from the tomography model

199   MeRE2020 from El-Sharkawy et al., (2020) is converted using a constant conversion factor (ζ)

200   of 0.3. The converted relative density distribution varies between -240 and 350 kg/m^3. High

201   correlations between the structural pattern in the converted density distribution and the relative

202   seismic velocities are observed (Fig. 3), the similarity in the structure pattern is expected due

203   to the linear relationship we introduced here. The converted 3D relative density distribution

204   reflects the variation of seismic velocities in the Alpine lithosphere and therefore includes the

205   heterogeneities of the subduction slab segments, as seen by the tomographic models (Fig 3).

206   The relative density model is transferred into tesseroids with a horizontal expansion of 0.2° and

207   a vertical expansion of 3 km. The Tesseroid model is forward calculated in order to estimate the

208   gravity response of the converted density distribution of the Alpine lithosphere in the depth

209   interval of 70 km to 200 km. No horizontal extensions of the mantle model are introduced

210   because relative densities are used and therefore edge effects are not expected to be significant

211   and would only affect the outer most degrees of the model. The slab segments are located central

212   in the model far away from possible artifact due border effects.

213
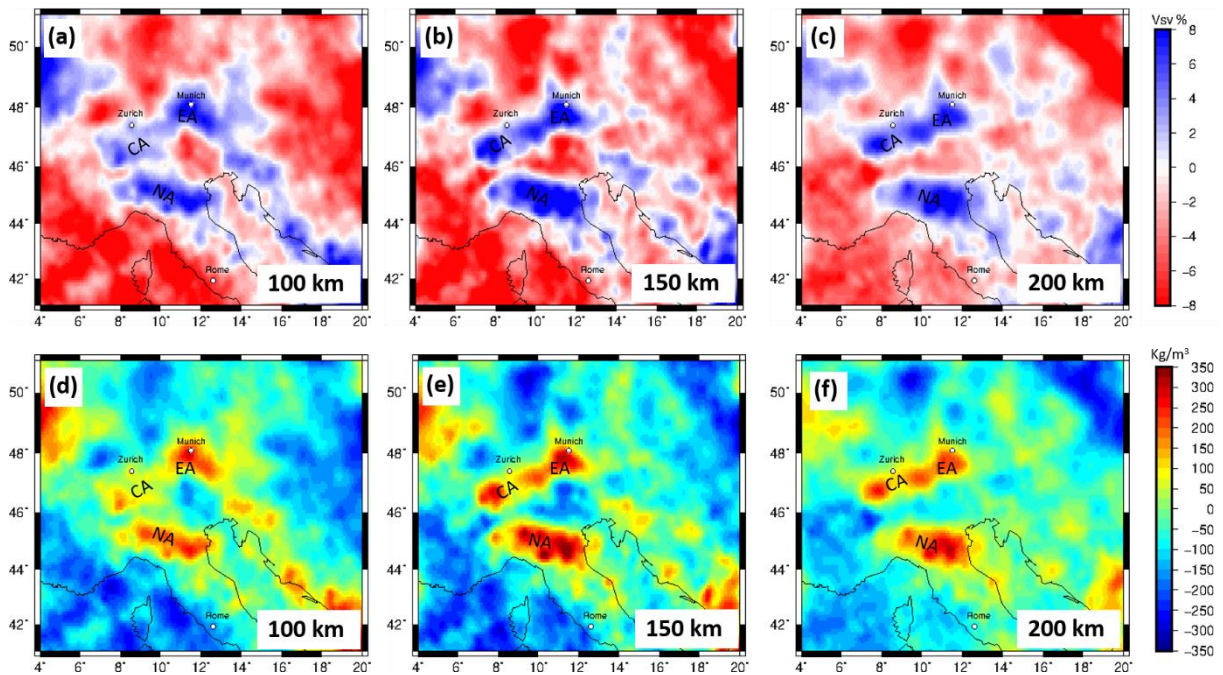
Figure 3 **(a)-(c)** Depth slices of relative surface wave velocities (Vsv) from MeRE2020 (El-Sharkawy et al., 2020). **(d)-(f)** converted relative density distribution in different depths based on a conversion factor (ζ) of 0.3. CA = Central Alpine Slab; EA = Eastern Alpine Slab; NA = Northern Apennine Slab

3.1 Results

In the forward calculated gravity field, a gravity high with a magnitude of ~40 mGal is observed

over the Alps (Fig. 4). That might be interpreted as relating to the proposed slab segments in

the Northern Apennine and Alpine area. However, the gravity field (and gradients, see appendix)

is dominated by anomalies outside the Alpine realm (Fig. 4), for instance in the Ligurian Sea

and the Dinaride-Hellenide Orogen. Therefore, in the next step, we try to concentrate on the

seismic anomalies in the Alpine realm that can be related to the slab segments.
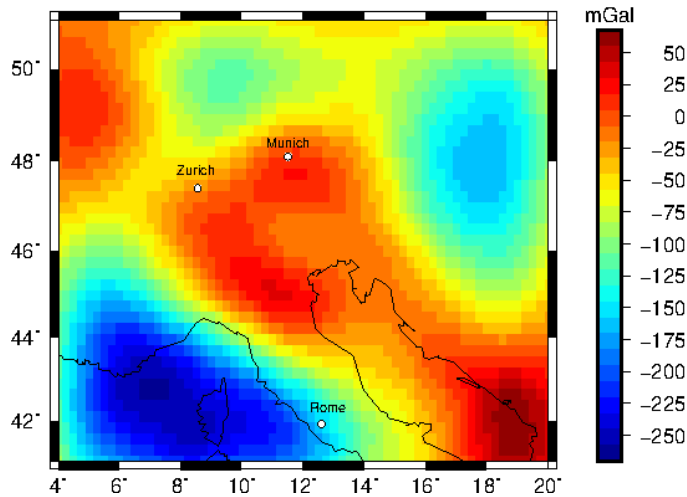
225

226 *Figure 4 Forward calculated gravity signal from relative density distribution converted from relative seismic velocities using*
227 *a conversion factor of 0.3 at a station height of 6040m.*

4 Slab models

229 To estimate the gravity contribution of independent slab segments we introduce different

230 models for the subducting lithosphere. First, we use a set of models with simple constant density

231 distribution in the slab, where the parameters, namely the density contrast and thickness of the

232 slab segment is varied (approach 2). Secondly, we create a set of slab models accounting for

233 compositional and thermal variations with depth (approach 3). Those models of approach 3 are

234 created with the software package LitMod 3D (Fullea et al., 2009) and here the slabs are strictly

235 vertical due to software limitations. Slab models created within LitMod will be referred as

236 LitMod models in the following. For all non-LitMod models, the gravity and gravity gradients

237 are calculated using tesseroids, which are spherical prisms (Uieda et al., 2016).

4.1 Slab modelling with constant density contrast and slab thickness

239 We define two alternative slab configurations based on crustal thickness model by Spada et al.

240 (2013) and several different tomographic studies, see detailed description of the slab

241 configurations below. At different depths, isolines are picked in the Moho depth map and

242 tomographic images, defining the upper boundary of subducting slab segments. The isoline of

243 the crust mantle boundary (Moho interface) is used as an onset of the slab to the crust and

244 defines the upper boundary of the subduction slab segment. At upper mantle depth, increased

245   seismic velocity anomalies in tomographic models beneath the Alps are interpreted as contrast

246   between colder and therefore denser subducting material to the surrounding mantle material. At

247   100, 150, and 200 km depth, the upper boundary of the slab segment is defined at the 0%

248   contour line of the relative seismic velocity, marking the transition from rocks with low velocity

249   to high velocity rocks. The isolines at the Moho interface, 100 km, 150 km and 200 km depth

250   are displayed upon the Alpine topography (Fig. 5 a-b) Vertical interpolation between the upper

251   boundary isolines at different depths (Moho depth, 100, 150 and 200 km) define a continuous

252   surface of the upper slab boundary. The lower boundary of the slabs and therefore the thickness

253   of the slab segment is not picked based on seismic data but assumed to have constant

254   thicknesses for simplifications. The thickness is varied for different models from 60 to 100 km

255   depth.

256
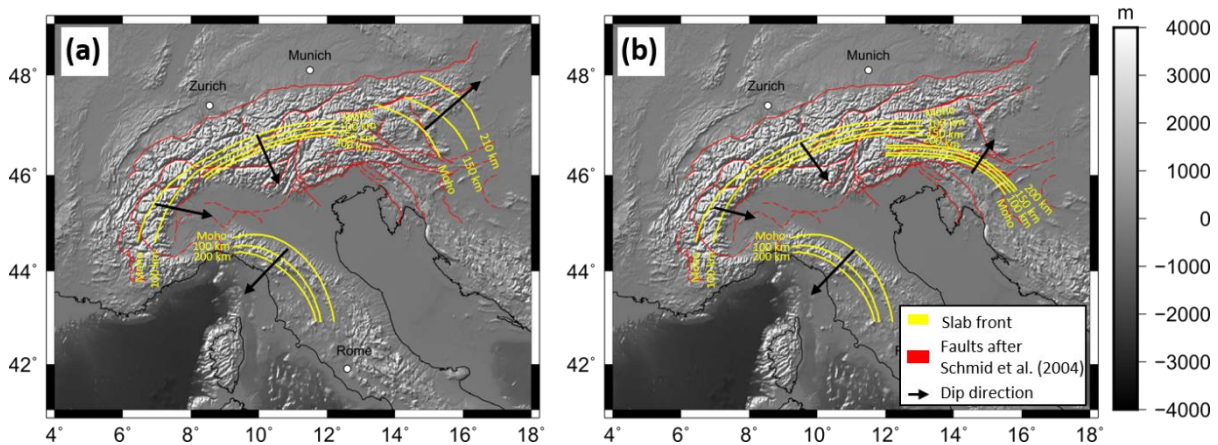
*Figure 5 Defined isolines based on crustal thickness estimations and seismological tomography models for the upper slab boundary for **(a)** Configuration 1 and **(b)** Configuration 2. Black arrows indicate the subduction direction. In red the fault configuration after Schmid et al. (2004).*

260   3.1.1 Alternative slab configurations

261   We define two different slab configurations. Configuration 1 (Fig. 5a) features a northeast

262   subducting slab segment in the Eastern Alps based on Lippitsch et al. (2003). A Central Alpine

263   slab segment is defined based on Lippitsch et al. (2003) and MeRE2020 (El-Sharkawy et al.,

264   2020) subducting in south-southeast direction. The Eastern and Central Alpine slab segments

265   are separated by a slab gap and show perpendicular subduction directions. The east-southeast-

266   ward subducted slab segment in the Western Alps is defined using the tomographic model of

267   Kästle et al. (2018), supporting the idea of slab break-off at about 100 km depth. Only attached

268   slab segments are considered, ignoring potential mantle upwelling in the break off zone and

269   neglecting the potentially remaining detached slab segment in larger depths. In addition, a

270   southwest-subducting slab segment beneath the northern Apennines is considered down to

271   about 200 km depth, as imaged by MeRE2020 (El-Sharkawy et al., 2020) because of its

272   proximity to the western Alps.

273   Configuration 2 (Fig. 5b) considers a slab configuration mainly based on the interpretation of

274   the MeRE2020 model (Fig. 3) by El-Sharkawy et al. (2020). In the Eastern Alps, both a short

275   southward subducting Eurasian slab segment as well as a short northward subducting Adriatic

276   slab are assumed. The Central and Western Alpine slab segments as well as the slab beneath the

277   northern Apennines are identical to Configuration 1.

278   4.1.2 Forward calculation

279   To estimate the gravity effect of the slab configurations, the geometries are discretized into

280   tesseroids with a 0.2° extension in the horizontal domain and a vertical size of 20 km. The

281   tesseroids range from 40 km to 200 km depth. First, a constant density contrast is assigned to

282   the entire slab. We test density contrasts from 20 kg/m^3 to 80 kg/m^3. The thickness of the Alpine

283   slab is not well constrained. We test for three slab volumes by assigning three slab thicknesses,

284   60 km, 80 km and 100 km based on studies on other subducting slab segments (e.g. Wang et

285   al., 2020). Due to the curved geometries of the proposed slab segments rectangular tesseroids

286   with a horizontal expansion of 0.2° will either over- or under-estimate the volume of a

287   subducting slab at the edges of the slab. The percentage volume share of each tesseroid to the

288   slab geometry is calculated. The assigned density contrast of the tesseroids which does not lay

289   fully within the slab geometry is decreased according to the percentage volume within the slab

290   geometry. Therefore, the density distribution correlates to the hypothetical slab positions and

291   volumes in the Alpine subsurface without increasing the discretisation resolution of the

292   tesseroid model beyond the uncertainty of gravity measurements and seismic tomographies.

293   The offset between the 40 km upper tesseroid boundary to the slab onset at the crust in 44 km

294   depth is corrected using the same process.

295   4.1.3 Results
296   Forward calculated slab models for predefined slab geometries of Configuration 1 and 2 with a

297   constant density contrast of 60 kg/m^3 and a constant thickness of 80 km result in a sharp gravity

298   signal ranging from 70 mGal to 100 mGal (Fig. 6). Both models generate gravity signals in the

299   order of magnitude of 70 mGal in the Central Alpine region as well as in the Apennine. The

300   gravity signal in the Eastern Alps differ for the two hypotheses (Fig. 6 a, b). The Western Alpine

301   slab segment shows the weakest signal in both models.

302
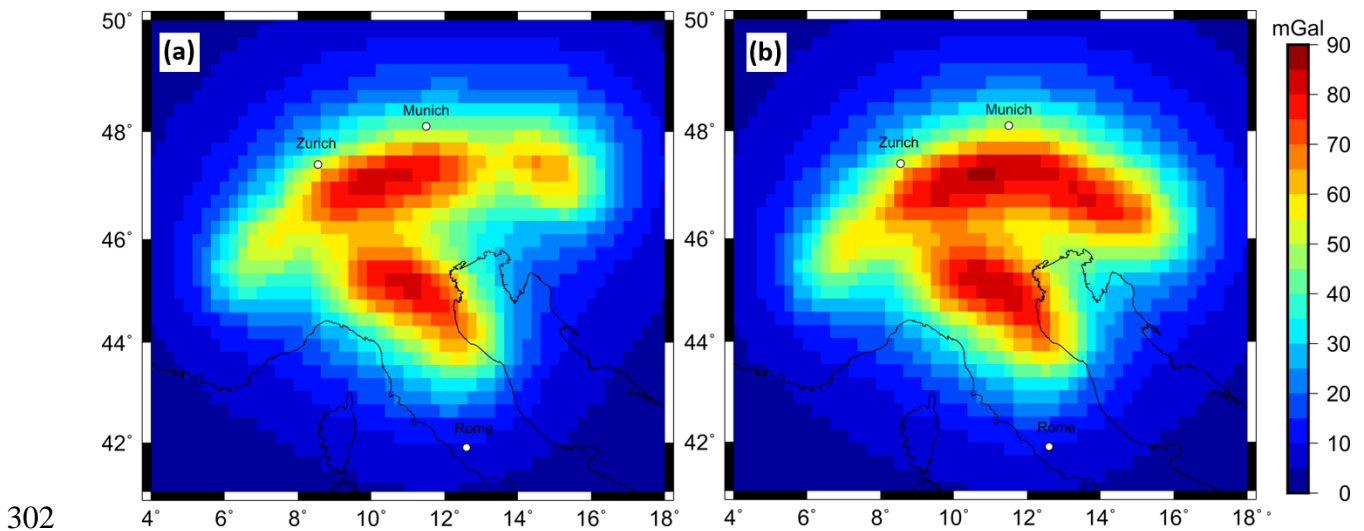
303   *Figure 6 Forward calculated gravity disturbance signal at a station height of 6040 m for predefined sub-crustal slab geometries*
304   *with a content density contrast of 60 kg/ m^3 and a constant thickness of 80 km. (a) predefined slab configuration 1 (b) predefined*
305   *slab configuration 2.*

306   The gravity signal ranges from 30 to 110 mGal depending on the assigned density contrast and

307   thickness for both slab geometry models (Fig. 7). The highest magnitude of forward calculated

308   gravity signal is in the order of 110 mGal and is observed for a slab model with a density

309   contrast of 80 kg/m^3 and a constant slab thickness of 100 km, while the lowest signal is

310   produced by a combination of 20 km/m^3 density contrast and a slab thickness of 60 km. Similar

311   gravity response is produced by different combinations of density contrast and volume. The

312   signal pattern is influenced by the predefined slab geometry, while the magnitude of the gravity

313   signal is depending on the density contrast and thickness (Fig. 7).

314
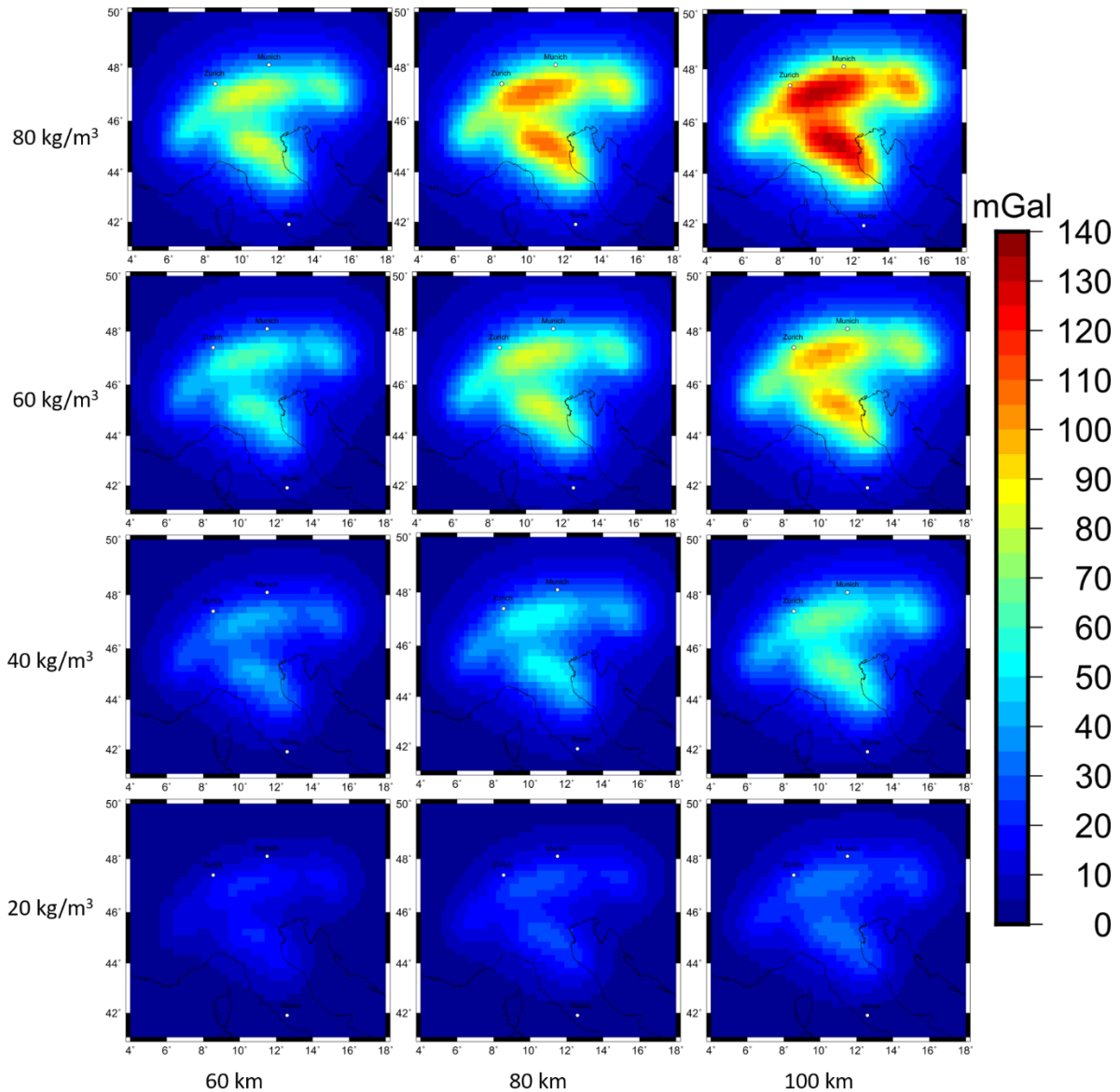
Figure 7 Forward calculated gravity disturbance signal for 12 different combination of density contrast and slab thickness for
315
sub-crustal slab configuration 1 at a station height of 6040 m.
316

317   Forward calculated gravity gradients at satellite height show the same dependency of signal

318   strength (see Appendix). The forward calculated gravity field of approach 2 differs significantly

319   from the forward calculated gravity field of the complete mantle density inhomogeneity of

320   approach 1 (Fig. 4), which only reaches a positive mantle effect of maximum 50 mGal.

321   **4.2 Geophysical and petrological modelling with LitMod**

322   For modelling the Alpine slab segments taking temperature and pressure variations as well as

323   composition of the lithosphere and sub lithosphere into account, the geophysical and

324   petrological modelling software LitMod 3D is utilized (Fullea et al.,2009). LitMod 3-D is a

325 finite difference code, which allows the modelling of lithospheric and sub lithospheric

326 structures down to 400 km depth by solving the heat transfer, thermodynamical, rheological,

327 geopotential, and isostasy equations (Afonso et al., 2008; Fullea et al., 2010).

328 A LitMod model consists of a set of crustal, lithospheric- and sub lithospheric layers

329 characterized by their petrophysical and thermal properties, which are used as input data (Fullea

330 et al., 2010). LitMod provides as an output i.e. the density -, temperature-, pressure- distribution

331 as well as the forward calculated gravity disturbance and gravity gradients (Fullea et al. 2009).

332 The assigned composition for the different layers is calculated using a LitMod subroutine which

333 utilizes the Perple_X algorithm of Connolly (2009). Perple_X calculates in the LitMod

334 implementation the specific bulk rock properties based on the six main lithospheric oxides

335 (SiO_2, Al_2O_3, FeO, CaO, Na_2O) by minimizing Gibbs free energy equation. The Alpine

336 lithosphere and sub lithosphere as well as the proposed slab segments are modelled using

337 standard global lithospheric and sub lithospheric compositions to test the influence of

338 compositional variations within the slab segments on the gravitational signal. Here, we use the

339 so-called Tecton and Proterozoic type-composition (Table 1). Those compositions were chosen

340 for a model with a homogeneous crust, lithosphere and sub-lithosphere, where the density

341 changes as a function of temperature and pressure based on the assigned compositions. The

342 different slab composition is introduced to test whether a compositional contrast, in addition to

343 the expected thermal difference, results in a significant density contrast between the slab and

344 the surrounding material.

345 *Table 1: Mineralogical composition for the lithospheric and sub lithospheric structure.*

Major Oxide Compositions	Aver. Tecton Gnt. SCLM [a]	Aver. Tecton Gnt. Peridotite [a]	Average Proterozoic Massif	PUM [b]	DMM [c]
SiO_2	44.5	45	45.2	45	44.7
Al_2O_3	3.5	3.9	2	4.5	3.98
FeO	8	8.1	7.9	8.1	8.1

MgO	39.8	38.7	41.6	37.8	37.8
CaO	3.1	3.2	1.9	3.6	3.17
Na$_2$O	0.26	0.24	0.13	0.36	0.13

346 [a] Classifications according to Griffin et al. (1999b), [b] McDonough & Sun (1995), [c] Workman & Hart (2005) DMM = Depleted

347 mid-oceanic ridge basalt mantle, PUM = primitive upper mantle.

348 First, we create a reference model (M$_0$) without a slab segment. This model contains topography

349 from the ETOPO1 dataset (Amante and Eakins, 2009), the Moho depth from Spada et al. (2013)

350 and Grad et al. (2009). The lithosphere asthenosphere boundary (LAB) is a required interface

351 for the LitMod 3D to divide the model between the lithosphere and sub lithosphere and to assign

352 compositions. We introduce a fixed technical LAB at a depth of 100 km throughout the model

353 despite of the presence of slabs as the LAB is defined as the 1300°C isotherm. This set-up avoids

354 that the isotherm follows the geometrical shape of the slab, which would lead to a location in

355 unrealistic large depths (>200 km). In addition, we neglect the topography of the LAB for

356 several reasons: i) the information of the lithospheric thickness in the Alpine forelands is spare

357 and under ongoing discussions, ii) the fixed depth value is based on thermal isostasy LAB

358 estimations from Artemieva et al. (2019), which shows a LAB depth in the range of 80 to 120

359 km depth in the Alpine forelands. This technical LAB is used to parameterize the model and is

360 not meant to represent the topography of the LAB. The modelled slab segments are extending

361 vertically downwards.

362 Slab segments are introduced stepwise for the lithosphere and sub lithosphere domains into the

363 model as well as thermal anomalies for the slab segment beneath the technical LAB, which

364 describes the 1300°C isotherm (Table 2). Calculating the difference to the reference model (M$_0$)

365 allows to estimate the effect a slab segments has on the density, temperature distribution of the

366 Alpine subsurface and therefore on the Alpine gravity field based on slab position, slab

367 geometry and composition.

368 *Table 2: Different LitMod models and there incorporated lithospheric and sub lithospheric structures and compositions.*

Models	Slab geometries	Slab composition (mantle)	Mantle composition	Slab composition (sub lithosphere)	Sub lithosphere composition	Thermal anomaly within sub lithospheric slab
M_0	-	-	aver. Tecton Gnt.	-	PUM	-
M_1	Configuration 1	Aver. Tecton Gnt. Peridotite	aver. Tecton Gnt.	-	PUM	-
M_2	Configuration 2	Aver. Tecton Gnt. Peridotite	aver. Tecton Gnt.	-	PUM	-
M_3	Configuration 1	Aver. Tecton Gnt. Peridotite	aver. Tecton Gnt.	DMM	PUM	-100 °K
M_4	Configuration 2	Aver. Tecton Gnt. Peridotite	aver. Tecton Gnt.	DMM	PUM	-100 °K
M_5	Configuration 1	Aver. Tecton Gnt. Peridotite	aver. Tecton Gnt.	PUM	PUM	-
M_6	Configuration 1	Aver. Tecton Gnt. Peridotite	aver. Tecton Gnt.	DMM	PUM	-
M_7	Configuration 1	Aver. Tecton Gnt. Peridotite	aver. Tecton Gnt.	DMM	PUM	-200 °K
M_8	Configuration 2	Average Proterozoic Massif	aver. Tecton Gnt.	-	PUM	-

369 A positive density contrast between subducting material and the surrounding mantle material

370 results in a negative buoyancy force. A density contrast is introduced into the LitMod model by

371 a difference in composition between the subducting denser slab and the surrounding mantle

372 (Fig. 9). Here, we use Tecton like compositions for the lithosphere and the subducting slab

373 segments since the Alpine slab segments result from continent-continent collision (Tables 1 and

374 2). A later model features a Proterozoic slab composition (M_8). Depleted mid-oceanic ridge

375 basalt mantle (DMM) and primitive upper mantle (PUM) are used for the sub lithospheric

376 domain. Additional to the density contrast within the sub lithosphere, a temperature anomaly of

377 – 100 K is introduced for the sub lithospheric part. Later models include a variation of

378 temperature anomalies (M_5, M_6, M_7). Note those compositions are used as a first order test and

379 serve as a starting point for synthetic slab models to illustrate the compositional and thermal

380 effect on the gravity signal by influencing the density distribution. They do not necessary

381 represent the compositional mantle environment in the Alpine region.
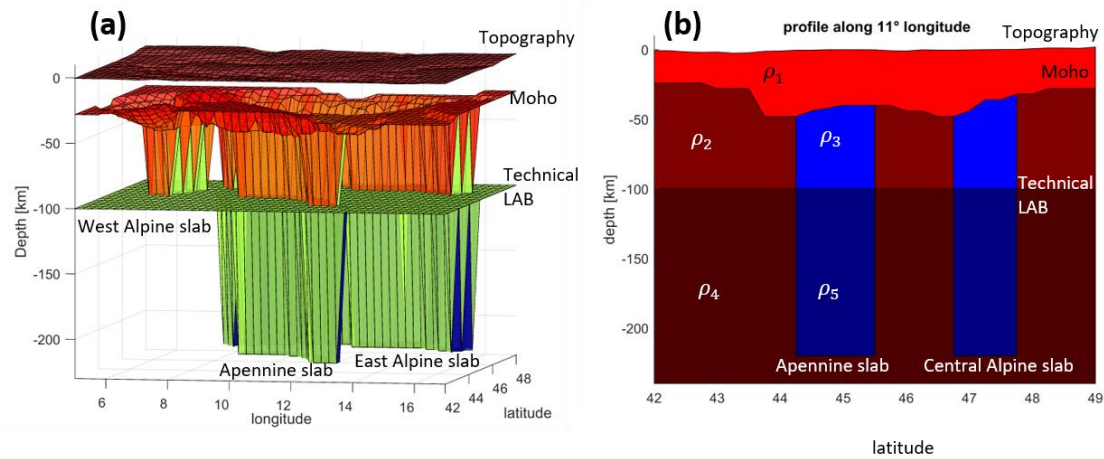
Figure 8 (a) 3D model set up using LitMod 3D. Topography, Moho and LAB depth as well as the vertical incorporated slab models are used as input layers with assigned petrophysical and thermal properties. (b) Profile along 11° longitude through a LitMod model containing Topography, crustal and lithospheric thickness as well as a slab segment. rho_{1-5} indicate petrophysical and thermal property variations for each layer.

4.2.1 Results

The gravity signal of the predefined slab segments is forward calculated as well as the background model without incorporation of slab segments. The residual between both forward calculations gives the gravitational contribution of the slab segments, while other gravitational effects, like the topography or crustal thickness variation and mantle variations outside the slab are not considered.

A slab segment with an average Tecton Gnt. composition (M_1, M_2) results in a slightly denser material compared to the surrounding mantle (M_0), while a slab segment with a Proterozoic composition (M_8) shows a less dense lithospheric structure compared to the reference model (M_0), this composition results in less dense slab segment, which would not be subducted due to the positive buoyancy (Fig. 10). However, we aim to illustrate the effect composition has on the density distribution within the slab and to the surrounding mantle and show the importance of correct compositional information, therefore we focus on the difference in density contrast between slab and surrounding mantle and neglecting the sign of the density contrast.
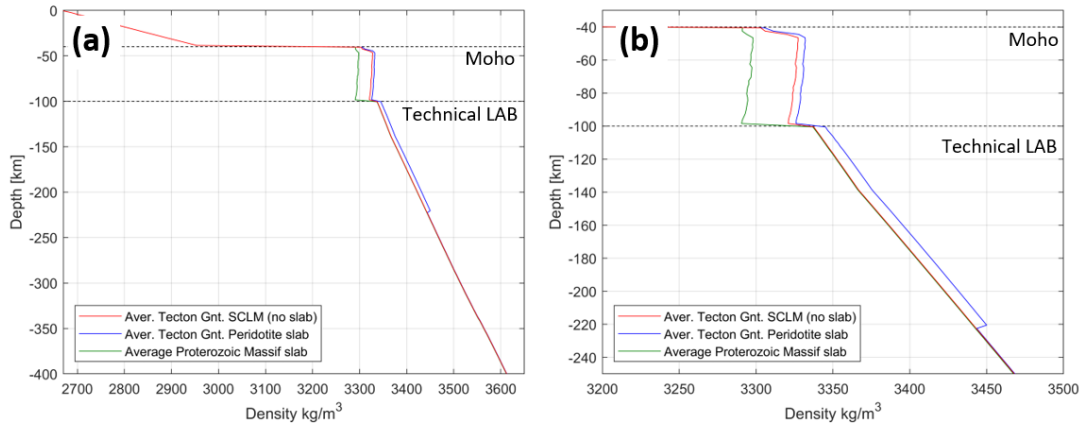
Figure 9 (a) density profile at 11° longitude and 45° latitude for the full vertical model space of 400 km depth. Density profiles for 3 different models (M0, M1, M9) with different compositional properties are shown. (b) Zoomed in profile at the depth range of present slab segments.

The difference in density distribution (density contrast) within the slab segments with a Tecton composition (M_1, M_3) to the reference model (M_0) is in the order of 5 kg/m^3 for the lithosphere and in the order of 10 kg/m^3 for the sub lithospheric domain (Fig. 10a). The density variations within the lithospheric and sub lithospheric slab domain are less than 1 kg/m^3 resulting from both depth dependent variations in pressure and temperature. Between lithosphere and sub lithosphere, a rapid increase in density contrast is observed (Fig. 10a). The density contrast of a lithospheric Proterozoic slab composition (M_9) to the reference model (M_0) is in the order of -30 kg/m^3 (Fig. 10b).
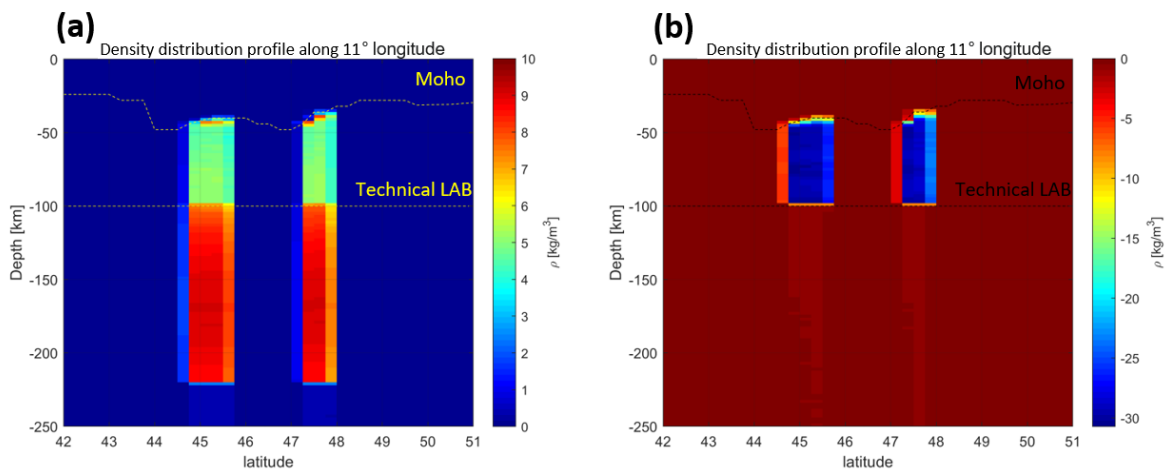
Figure 10 (a) residual density contrast for lithospheric and sub lithospheric slab segments of model (M3) with Tecton like composition within the lithosphere and PUM and DMM composition in the sub lithosphere with an additional thermal anomaly of -100° k for the sub lithospheric slab segment to the background model (M0). (b) Residual lithospheric density contrast of a Proterozoic lithospheric slab segment (M8) to a Tecton compositional surrounding mantle (M0). Residual density contrast is limited to the technical LAB as the sub-lithospheric part is identical to the reference model (see also Fig. 9b)

419   The gravity signal caused by the proposed slab segment configurations is estimated for

420   lithosphere and sub lithosphere separately. The forward calculated gravity effect, at topographic

421   surface level, for the slab configuration 1 for the lithospheric part is in the order of 4 mGal

422   while the sub lithospheric gravity signal is in the range of 7 mGal (Fig. 12a, b). The combined

423   gravity signal is in the order of 12 mGal (Fig. 12c). The gravity signal in the Eastern Alps for

424   Configuration 2 is significantly larger in the order of 17 mGal for the combined model (Fig.

425   12f).

426
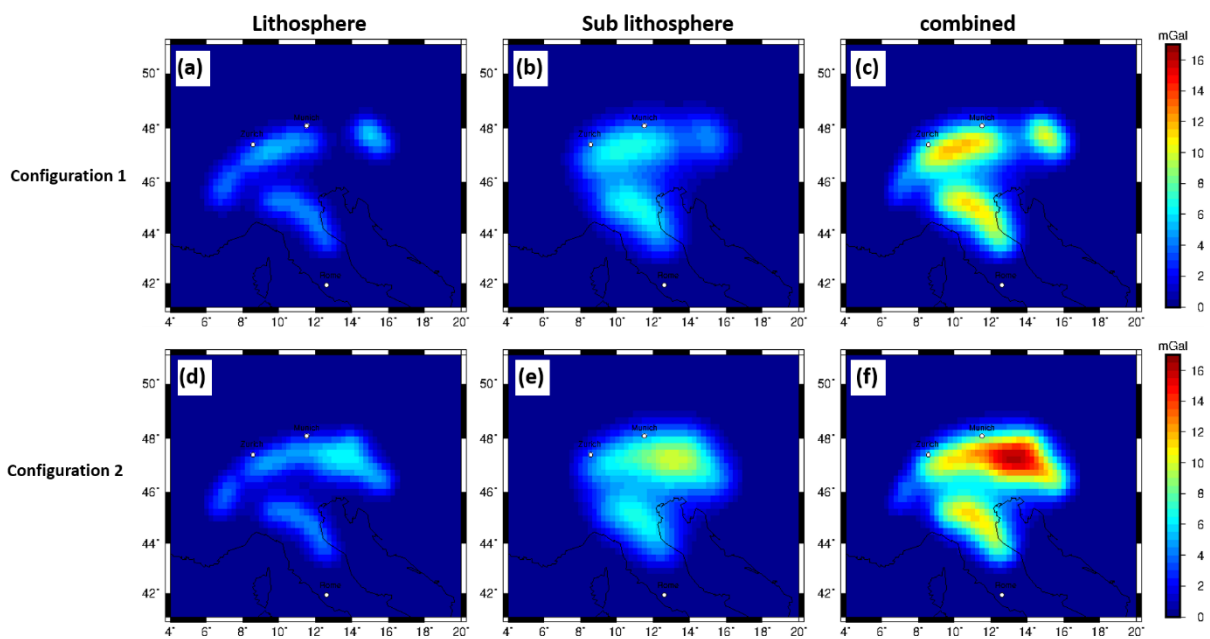
Figure 11 Residual of the forward calculated gz gravity signal of lithospheric slabs at surface station height based on LitMod
models with Tecton like compositions in the lithosphere and PUM and DMM compositions in the sub lithosphere (M_1, M_2, M_3,
M_4,) with an additional thermal anomaly of -100° k for the sub lithospheric slab segment, for predefined slab Configuration to
*the background model (M_0). **(a)-(c)** Configuration 1. **(d)-(f)** Configuration 2. Crustal and topographic contribution are nullified.*

431   The calculated gravitational effect of a slab segment with Proterozoic composition and a Tecton

432   surrounding mantle composition is in the order of -40 mGal for the gz component (Fig. 12 a).
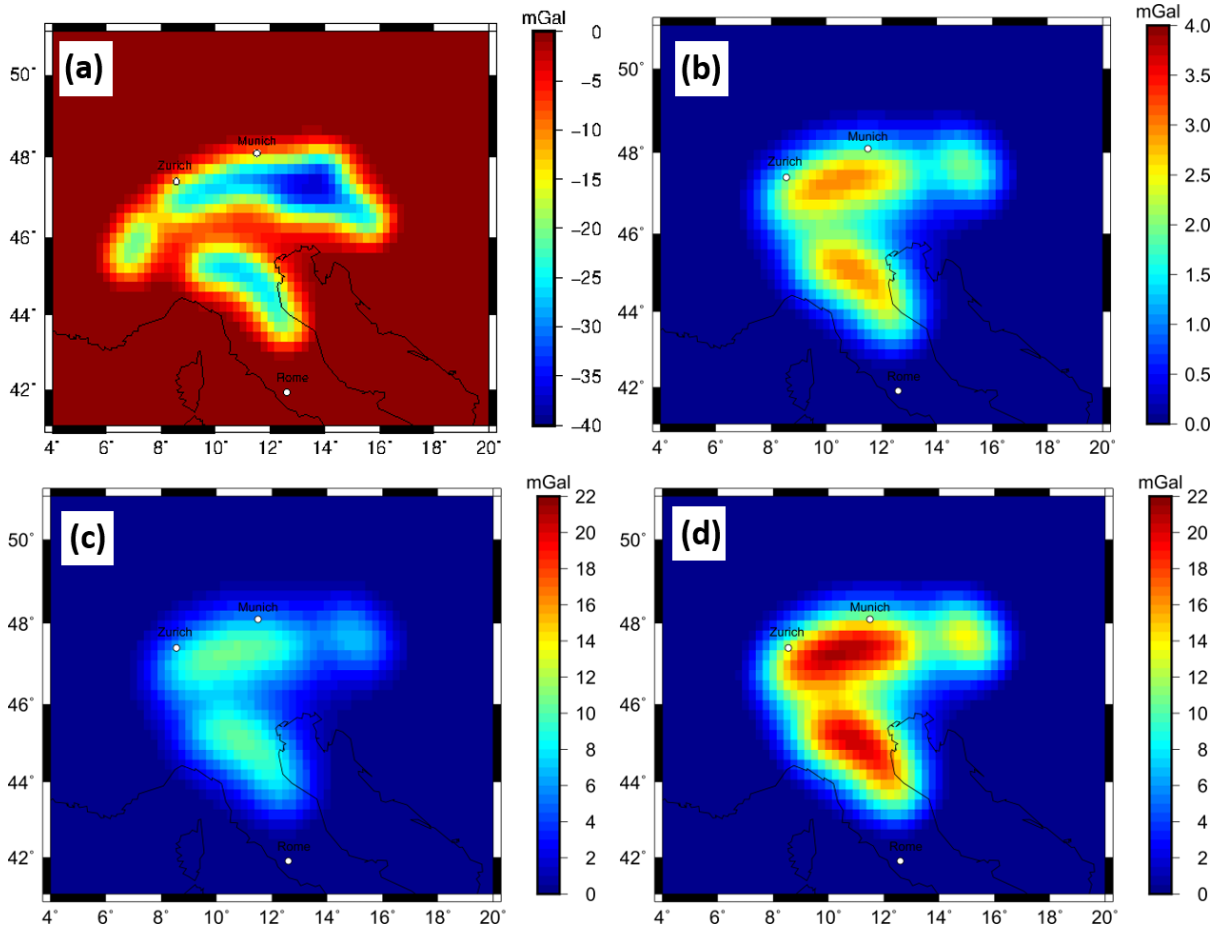
*Figure 12 **(a)** Forward calculated gravity effect of a Proterozoic lithospheric slab segment to a Tecton compositional surrounding mantle for configuration 2, obtained by calculating the residual between M_8 and M_0. **(b)** gravity signal produced by purely compositional effect in the sub lithosphere between a PUM and DMM composition, obtained by calculating the residual between M_5 and M_6. **(c)** gravity signal produced by purely thermal anomaly of -100° K for a sub lithospheric slab segment, obtain by calculating the residual between M_3 and M_6. **(d)** gravity signal produced by purely thermal anomaly of -200° K for a sub lithospheric slab segment obtained by calculating the residual between M_6 and M_7.*

The gravity response to a compositional variation within the sub lithosphere between the incorporated slab segment (DMM composition) and the surrounding mantle (PUM composition) is in the order of 4 mGal (Fig. 12b). The gravity response for a pure thermal anomaly of -100 K within the sub lithospheric slab segment is in the order of 16 mGal (Fig. 12c), while a pure thermal anomaly of -200 K within the sub lithospheric slab segment is in the order of 21 mGal.

5 Discussion

The imprint of the gravity response caused by the density distribution based on direct conversion of seismic velocities (approach 1) is visible, however, individual and independent slab segments cannot be identified (Fig. 4). The strength of this approach is that it is fast to

449   implement and can provide a first order characterization of the gravity signal and slab

450   geometries of subducting lithosphere. However, a clear characterization of subducting slab

451   segments is not possible. First of all, the density model depends on the resolution and

452   regularization of the seismological model, which can lead to distortions in the gravity response

453   (e.g. Root, 2020). The method is dependent on the choice of the conversion factor and might

454   overestimate the density (see the large negative anomaly in the Ligurian Sea). The conversion

455   factor is a strong simplification of nature and for such a geodynamic complex area, a constant

456   conversion factor is not adequate.

457   The forward calculated gravity field with competing predefined slab geometries (approach 2)

458   shows a clear gravity signal, where the individual slab segments are distinguishable (Fig. 6).

459   A relative gravity low related to the slab gap in the Eastern Alps is a prominent feature in the

460   gravity signal of Configuration 1 (Fig. 6a). The eastern Alpine slab segment of Configuration

461   1, due to its relatively small volume, result in a lower signal compared to the Central Alpine

462   slab segment.

463   Configuration 2 shows a larger gravity signal in the Eastern Alps up to 100 mGal (Fig. 6b)

464   compared to Configuration 1. The increase of the gravity signal is attributed to the subduction

465   of both Eurasian and Adriatic lithosphere in the Eastern Alps. The gravity signal shows a

466   continuous transition from the Central Alps to the Eastern Alps, where the contribution of the

467   destined slab segment cannot be distinguished in the resulting gravity field (Fig. 6b). In the

468   Western Alps, Configuration 1 and 2 show a lower gravity signal compared to the Central Alps.

469   This is attributed to the much shallower Western Alpine slab segment that penetrate down to

470   100 km depth.

471   The gravity signal is influenced by both the assigned density contrast and thickness of the slab.

472   A trade of between both parameters is clearly observable as the same gravity response of the

473   slab configuration can be achieved with different values of density contrast and slab thickness.

474   Therefore, making it impossible to derive slab properties in form of density contrast and slab

475   thickness from the gravity field (Fig. 7).

476   The calculated densities in LitMod 3-D models (approach 3) are estimated taking temperature

477   and pressure variations into account based on an assigned composition. The composition has a

478   strong influence on the resulting density contrast. In the case that the compositional contrast

479   between slab segment and surrounding mantle is small, the density contrast is consequently

480   small as well (Fig. 9 and 10a). With increasing compositional differences, the density contrast

481   increases as well. A strong density contrast within the slab segment is recognizable between

482   lithospheric and sub lithospheric domain (Fig. 10a and b), while the variations between the slab

483   and surrounding mantle remain small.

484   The gravity signal shows in the Eastern Alps significant larger signal from the lithosphere and

485   sub lithosphere domain for Configuration 2 (Fig. 11d, e, and f) compared to Configuration 1

486   (Fig. 11a- c). The different slab segments are distinguishable with the exception of the two slab

487   segments in the Eastern Alps in Configuration 2 (Fig. 11). The contribution from the

488   lithospheric domain to the gravity signal is smaller than from the sub lithospheric domain (Fig.

489   11b, and e). However, the slab gap and the eastern slab segment feature can be recognized in

490   the lithospheric part in Configuration 1 but not in the gravity signal of the full model.

491   The Proterozoic slab segment has a larger gravity response compared to the Tecton-like

492   composition. This gravitational signal is negative due to the less dense Proterozoic composition

493   in comparison to the reference model (M_0) (Fig. 12a).

494   Sub lithospheric composition has only a small influence on the gravity field, in the order of 4

495   mGal (Fig. 12b). However, a thermal anomaly within the sub lithospheric slab in the order of -

496   100K result in a gravitational response of 16 mGal (Fig. 12c) and for a -200 K anomaly in the

497   order of 21 mGal (Fig. 12d). Both the composition and the thermal variation influence the

498   density and consequently the gravity response. However, the thermal component is a much

499   larger contributor.

For the three approaches (section 3, 4.1 and 4.2) a measurable gravity effect of the subducting slab segments is observable. The independent slab segments are distinguishable to a certain degree with the exception of the bivergent slab configuration in the Eastern Alps (Fig. 6, and 11) and the model containing converted density from seismic velocities (Fig 4), while the slab configurations cannot be separated at satellite altitude (Appendix). Forward calculated gravity anomalies from converted density distribution suggest a gravitational signal of the slab segments in the order of 40 mGal which corresponds to a density contrast of 20 to 40 kg/m^3 in the models with predefined slab geometry. The models with a Tecton like composition suggest a gravity effect of the slab segments in the order of only 16 mGal, corresponding to a density contrast of 20 kg/m^3 in the simple model. Increasing the compositional difference with a Tecton composition suggests a gravity signal in order of 30 mGal and is in line with the converted density model.

All three methods show a positive gravity signal contribution, which can be related to sub-crustal density variations for approach 1 and to predefined sub-crustal slab segments for approach 2 & 3, up to 40 mGal to the Alpine gravity field. That is significant in comparison to the observed Bouguer Anomaly with a minimum of ~-200 mGal. If this contribution is not considered, a significant part of the gravity signal is attributed to crustal thickness or intra-crustal sources. Due to the long-wavelength appearance of the gravity effect, that might not be relevant for small-scale or local studies, the effect is only seen as a shift. For gravity models of larger areas (e.g. Eastern Alps) or even the entire regions that should not be neglected. For one, estimates of crustal thickness or the mass distribution are significantly biased, and placing the Alps in the geodynamic context of the surrounding requires a careful and complete consideration of all sources in order to provide realistic density distribution required for geodynamic models (e.g. Reuber et al., 2019).

6 Conclusions

525   We have addressed the potential gravity effect of proposed slab segments in the Alpine region

526   using three different modelling approaches.

527   •   Converted density from seismic tomography: In the resulting gravity signal the imprint

528   of slab segments is visible, however, distinguishing between the different and

529   independent slab segments is not possible.

530   •   Models with predefined slab segments are dependent on the assigned density contrast

531   and volume as well as on the predefined positions of the slab segments. The gravity

532   signal caused by the slab segments are sharp and can be separated for the different slab

533   segments for the gravity field at the surface. Significant gravity contributions from slab

534   segments below 200 – 250 km to the Alpine gravity are unlikely.

535   •   Combined petrophysical-geophysical modelling results in the most complex models.

536   The calculated density variation within the slab is rather small compared to the density

537   contrast between lithosphere and sub lithosphere. The density distribution within the

538   slabs, and consequently the gravity field, is highly influenced by the slab composition

539   and thermal structure.

540   Sub-crustal density variation (approach 1) and predefined slab segments (approach 2 & 3)

541   suggest a positive sub-crustal gravity contribution of up to 40 mGal. Even though this might be

542   considered as a maximum gravity estimation of slabs, this value is significant, even compared

543   to the observed Bouguer Anomaly low of -200 mGal along the Alps. The interpretation of

544   density variation in the mantle in terms of subducting slab structures is a means to provide a

545   meaningful representation of the geodynamic complex Alpine area. For future studies correct

546   slab density structure are crucial to provide a representation of the Alpine geodynamic setting.

547   Precise estimations of the slab density structure require a correct crustal density and crustal

548   thickness model. With the integration of further observables, it might be possible to judge on

549   the correct slab configuration beneath the Alps. Furthermore, future studies based on the

AlpArray Network will be of high interest in better defining slab geometries as well as their properties.

Competing interests

The authors declare that they have no conflict of interest.

Author contributions

ML carried out the gravity modelling, visualized and interpreted the results and prepared the first manuscript draft. JE supervised the gravity modelling and interpretation, designed the original research project, acquisition of the financial support for the project leading to this publication and writing (reviewing and editing). TM defined the slab configurations based on tectonic and seismological knowledge and writing (reviewing and editing). AE created and provided the surface wave tomography model MeRE2020 and writing (reviewing and editing).

Acknowledgment

The authors thank the reviewers, Carla Braitenberg and an anonymous referee for their valuable suggestions, which helped to improve the manuscript significantly.

This study is part of the projects "Integrierte 3D Modellierung des Schwere- und Temperaturfelds zum Verständnis von Rheologie und Deformation der Alpen und ihrer Vorlandbecken - INTEGRATE" and "Surface Wavefield Tomography of the Alpine Region to Constrain Slab Geometries, Lithospheric Deformation and Asthenospheric Flow in the Alpine Region" funded by German Research Foundation (DFG) in the SPP Mountain Building Processes in 4D.

We thank the developer of open scientific Software which were utilized in this study: tesseroids (Uieda et al., 2016), LitMod 3D (Fullea et al., 2009 and Afonso et al., 2008) and Generic Mapping Tools (GMT) (Wessel et al., 2013; Wessel & Luis, 2017).

573   **References**

574   Afonso, J. C., Fernandez, M., Ranalli, G., Griffin, W. L., & Connolly, J. A. D. (2008). Integrated
575   geophysical-petrological modeling of the lithosphere and sublithospheric upper mantle:
576   Methodology and applications. Geochemistry, Geophysics, Geosystems, 9(5).
577
578   Amante, C., & Eakins, B. W. (2009). ETOPO1 arc-minute global relief model: procedures, data
579   sources and analysis.
580
581   Artemieva, I. M. (2019). Lithosphere structure in Europe from thermal isostasy. Earth-Science
582   Reviews, 188, 454-468.
583
584   Babuška, V., Plomerova, J., & Granet, M. (1990). The deep lithosphere in the Alps: a model
585   inferred from P residuals. Tectonophysics, 176(1-2), 137-165.
586
587   Beller, S., Monteiller, V., Operto, S., Nolet, G., Paul, A., & Zhao, L. (2018). Lithospheric
588   architecture of the South-Western Alps revealed by multiparameter teleseismic full-waveform
589   inversion. Geophysical Journal International, 212(2), 1369-1388.
590
591   Bouman, J., Ebbing, J., Fuchs, M., Sebera, J., Lieb, V., Szwillus, W., ... & Novak, P. (2016).
592   Satellite gravity gradient grids for geophysics. Scientific reports, 6(1), 1-11.
593
594   Braitenberg, C. (2015). Exploration of tectonic structures with GOCE in Africa and across-
595   continents. International Journal of Applied Earth Observation and Geoinformation, 35, 88-95.
596
597   Channell, J. E. T., & Horvath, F. (1976). The African/Adriatic promontory as a
598   palaeogeographical premise for Alpine orogeny and plate movements in the Carpatho-Balkan
599   region. Tectonophysics, 35(1-3), 71-101.
600
601   Connolly, J. A. D. (2009). The geodynamic equation of state: what and how. Geochemistry,
602   Geophysics, Geosystems, 10(10).
603
604   Dewey, J. F., Helman, M. L., Knott, S. D., Turco, E., & Hutton, D. H. W. (1989). Kinematics
605   of the western Mediterranean. Geological Society, London, Special Publications, 45(1), 265-283.
606
607   Ebbing, J., Braitenberg, C., & Götze, H. J. (2001). Forward and inverse modelling of gravity
608   revealing insight into crustal structures of the Eastern Alps. Tectonophysics, 337(3-4), 191-208.
609
610   Ebbing, J., Braitenberg, C., & Götze, H. J. (2006). The lithospheric density structure of the
611   Eastern Alps. Tectonophysics, 414(1-4), 145-155.
612
613   El-Sharkawy, A., Meier, T., Lebedev, S., Behrmann, J., Hamada, M., Cristiano, L., ... & Köhn,
614   D. (2020). The Slab Puzzle of the Alpine‐Mediterranean Region: Insights from a new, High‐
615   Resolution, Shear‐Wave Velocity Model of the Upper Mantle. Geochemistry, Geophysics,
616   Geosystems, e2020GC008993.
617
618   Fichtner, A., van Herwaarden, D. P., Afanasiev, M., Simutė, S., Krischer, L., Çubuk-Sabuncu,
619   Y., ... & Trampert, J. (2018). The collaborative seismic earth model: Generation 1. Geophysical
620   research letters, 45(9), 4007-4016.
621

Frisch, W. (1979). Tectonic progradation and plate tectonic evolution of the Alps. Tectonophysics, 60(3-4), 121-139.

Fullea, J., Afonso, J. C., Connolly, J. A. D., Fernandez, M., García-Castellanos, D., & Zeyen, H. (2009). LitMod3D: An interactive 3-D software to model the thermal, compositional, density, seismological, and rheological structure of the lithosphere and sublithospheric upper mantle. Geochemistry, Geophysics, Geosystems, 10(8).

Fullea, J., Fernàndez, M., Afonso, J. C., Vergés, J., & Zeyen, H. (2010). The structure and evolution of the lithosphere–asthenosphere boundary beneath the Atlantic–Mediterranean Transition Region. Lithos, 120(1-2), 74-95.

Ganguly, J., Freed, A. M., & Saxena, S. K. (2009). Density profiles of oceanic slabs and surrounding mantle: Integrated thermodynamic and thermal modeling, and implications for the fate of slabs at the 660 km discontinuity. Physics of the Earth and Planetary Interiors, 172(3-4), 257-267.

Götze, H. J., Lahmeyer, B., Schmidt, S., & Strunk, S. (1994). The lithospheric structure of the Central Andes (20–26 S) as inferred from interpretation of regional gravity. In Tectonics of the southern Central Andes (pp. 7-21). Springer, Berlin, Heidelberg.

Götze, H. J., & Krause, S. (2002). The Central Andean gravity high, a relic of an old subduction complex?. Journal of South American Earth Sciences, 14(8), 799-811.

Götze, H. J., & Pail, R. (2018). Insights from recent gravity satellite missions in the density structure of continental margins–With focus on the passive margins of the South Atlantic. Gondwana Research, 53, 285-308.

Grad, M., Tiira, T., & ESC Working Group. (2009). The Moho depth map of the European Plate. Geophysical Journal International, 176(1), 279-292.

Griffin, W. L., O'reilly, S. Y., Afonso, J. C., & Begg, G. C. (2009). The composition and evolution of lithospheric mantle: a re-evaluation and its tectonic implications. Journal of Petrology, 50(7), 1185-1204.

Gutknecht, B. D., Götze, H. J., Jahr, T., Jentzsch, G., & Mahatsente, R. (2014). Structure and state of stress of the Chilean subduction zone from terrestrial and satellite-derived gravity and gravity gradient data. Surveys in Geophysics, 35(6), 1417-1440.

Handy, M. R., Schmid, S. M., Bousquet, R., Kissling, E., & Bernoulli, D. (2010). Reconciling plate-tectonic reconstructions of Alpine Tethys with the geological–geophysical record of spreading and subduction in the Alps. Earth-Science Reviews, 102(3-4), 121-158.

Handy, M. R., Ustaszewski, K., & Kissling, E. (2015). Reconstructing the Alps–Carpathians–Dinarides as a key to understanding switches in subduction polarity, slab gaps and surface motion. International Journal of Earth Sciences, 104(1), 1-26.

Hawkesworth, C. J., Waters, D. J., & Bickle, M. J. (1975). Plate tectonics in the Eastern Alps. Earth and Planetary Science Letters, 24(3), 405-413.

672 Hetényi, G., Plomerová, J., Bianchi, I., Exnerová, H. K., Bokelmann, G., Handy, M. R., ... &
673 AlpArray-EASI Working Group. (2018). From mountain summits to roots: Crustal structure of
674 the Eastern Alps and Bohemian Massif along longitude 13.3 E. Tectonophysics, 744, 239-255.
675
676 Holzrichter, N., & Ebbing, J. (2016). A regional background model for the Arabian Peninsula
677 from modeling satellite gravity gradients and their invariants. Tectonophysics, 692, 86-94.
678
679 Hua, Y., Zhao, D., & Xu, Y. (2017). P wave anisotropic tomography of the Alps. Journal of
680 Geophysical Research: Solid Earth, 122(6), 4509-4528.
681
682 Isaak, D. G., Anderson, O. L., Goto, T., & Suzuki, I. (1989). Elasticity of single-crystal
683 forsterite measured to 1700 K. Journal of Geophysical Research: Solid Earth, 94(B5), 5895-
684 5906.
685
686 Isaak, D. G. (1992). High-temperature elasticity of iron-bearing olivines. Journal of
687 Geophysical Research: Solid Earth, 97(B2), 1871-1885.
688
689 Karato, S. I. (1993). Importance of anelasticity in the interpretation of seismic tomography.
690 Geophysical Research Letters, 20(15), 1623-1626.
691
692 Karousová, H., Plomerová, J., & Babuška, V. (2013). Upper-mantle structure beneath the
693 southern Bohemian Massif and its surroundings imaged by high-resolution
694 tomography. Geophysical Journal International, 194(2), 1203-1215.
695
696 Kästle, E. D., El-Sharkawy, A., Boschi, L., Meier, T., Rosenberg, C., Bellahsen, N., ... &
697 Weidle, C. (2018). Surface wave tomography of the alps using ambient-noise and earthquake
698 phase velocity measurements. Journal of Geophysical Research: Solid Earth, 123(2), 1770-
699 1792.
700
701 Kästle, E. D., Rosenberg, C., Boschi, L., Bellahsen, N., Meier, T., & El-Sharkawy, A. (2020).
702 Slab break-offs in the Alpine subduction zone. International Journal of Earth Sciences, 1-17.
703
704 Kincaid, C., & Olson, P. (1987). An experimental study of subduction and slab
705 migration. Journal of Geophysical Research: Solid Earth, 92(B13), 13832-13840.
706
707 Kissling, E., Schmid, S. M., Lippitsch, R., Ansorge, J., & Fügenschuh, B. (2006). Lithosphere
708 structure and tectonic evolution of the Alpine arc: new evidence from high-resolution
709 teleseismic tomography. Geological Society, London, Memoirs, 32(1), 129-145.
710
711 Kogan, M. G., & McNutt, M. K. (1993). Gravity field over northern Eurasia and variations in
712 the strength of the upper mantle. Science, 259(5094), 473-479.
713
714 Koulakov, I., Kaban, M. K., Tesauro, M., & Cloetingh, S. A. P. L. (2009). P-and S-velocity
715 anomalies in the upper mantle beneath Europe from tomographic inversion of ISC data.
716 Geophysical Journal International, 179(1), 345-366.
717
718 Le Breton, E., Handy, M. R., Molli, G., & Ustaszewski, K. (2017). Post-20 Ma motion of the
719 Adriatic Plate: New constraints from surrounding orogens and implications for crust-mantle
720 decoupling. Tectonics, 36(12), 3135-3154.
721

722 Lippitsch, R., Kissling, E., & Ansorge, J. (2003). Upper mantle structure beneath the Alpine
723 orogen from high-resolution teleseismic tomography. Journal of Geophysical Research: Solid
724 Earth, 108(B8).

726 Lüschen, E., Lammerer, B., Gebrande, H., Millahn, K., Nicolich, R., & TRANSALP Working
727 Group. (2004). Orogenic structure of the Eastern Alps, Europe, from TRANSALP deep seismic
728 reflection profiling. Tectonophysics, 388(1-4), 85-102.

730 Lüschen, E., Borrini, D., Gebrande, H., Lammerer, B., Millahn, K., Neubauer, F., ... &
731 TRANSALP Working Group. (2006). TRANSALP—deep crustal Vibroseis and explosive
732 seismic profiling in the Eastern Alps. Tectonophysics, 414(1-4), 9-38.

734 Lyu, C., Pedersen, H. A., Paul, A., Zhao, L., & Solarino, S. (2017). Shear wave velocities in
735 the upper mantle of the Western Alps: new constraints using array analysis of seismic surface
736 waves. Geophysical Journal International, 210(1), 321-331.

738 Mahatsente, R. (2019). Plate Coupling Mechanism of the Central Andes Subduction: Insight
739 from Gravity Model. Journal of Geodetic Science, 9(1), 13-21.

741 McDonough, W. F., & Sun, S. S. (1995). The composition of the Earth. Chemical geology,
742 120(3-4), 223-253.

744 McKenzie, D., & Fairhead, D. (1997). Estimates of the effective elastic thickness of the
745 continental lithosphere from Bouguer and free air gravity anomalies. Journal of Geophysical
746 Research: Solid Earth, 102(B12), 27523-27552.

748 Mitterbauer, U., Behm, M., Brückl, E., Lippitsch, R., Guterch, A., Keller, G. R., ... &
749 Šumanovac, F. (2011). Shape and origin of the East-Alpine slab constrained by the ALPASS
750 teleseismic model. Tectonophysics, 510(1-2), 195-206.

752 Nocquet, J. M., & Calais, E. (2004). Geodetic measurements of crustal deformation in the
753 Western Mediterranean and Europe. Pure and applied geophysics, 161(3), 661-681.

755 Piromallo, C., & Morelli, A. (2003). P wave tomography of the mantle under the Alpine‐
756 Mediterranean area. Journal of Geophysical Research: Solid Earth, 108(B2).

758 Reuber, G., Meier, T., Ebbing, J., El-Sharkawy, A., & Kaus, B. (2019, January). Constraining
759 the dynamics of the present-day Alps with 3D geodynamic inverse models-model version 0.2.
760 In Geophysical Research Abstracts (Vol. 21).

762 Root, B. C. (2020). Comparing global tomography-derived and gravity-based upper mantle
763 density models. Geophysical Journal International, 221(3), 1542-1554.

765 Schmid, S. M., Fügenschuh, B., Kissling, E., & Schuster, R. (2004). Tectonic map and overall
766 architecture of the Alpine orogen. Eclogae Geologicae Helvetiae, 97(1), 93-117.

768 Serpelloni, E., Vannucci, G., Anderlini, L., & Bennett, R. A. (2016). Kinematics,
769 seismotectonics and seismic potential of the eastern sector of the European Alps from GPS and
770 seismic deformation data. Tectonophysics, 688, 157-181.

771

772 Spada, M., Bianchi, I., Kissling, E., Agostinetti, N. P., & Wiemer, S. (2013). Combining
773 controlled-source seismology and receiver function information to derive 3-D Moho
774 topography for Italy. Geophysical Journal International, 194(2), 1050-1068.
775

776 Spakman, W., & Wortel, R. (2004). A tomographic view on western Mediterranean
777 geodynamics. In The TRANSMED atlas. The Mediterranean region from crust to mantle (pp.
778 31-52). Springer, Berlin, Heidelberg.
779

780 Spooner, C., Scheck-Wenderoth, M., Götze, H. J., Ebbing, J., & Hetényi, G. (2019). Density
781 distribution across the Alpine lithosphere constrained by 3-D gravity modelling and relation to
782 seismicity and deformation. Solid Earth, 10(6), 2073-2088.
783

784 Stampfli, G. M., & Borel, G. D. (2002). A plate tectonic model for the Paleozoic and Mesozoic
785 constrained by dynamic plate boundaries and restored synthetic oceanic isochrons. Earth and
786 Planetary Science Letters, 196(1-2), 17-33.
787

788 Tadiello, D., & Braitenberg, C. (2021). Gravity modeling of the Alpine lithosphere affected by
789 magmatism based on seismic tomography. *Solid Earth Discussions*, 1-31.
790

791 Tašárová, Z. A. (2007). Towards understanding the lithospheric structure of the southern
792 Chilean subduction zone (36 S–42 S) and its role in the gravity field. Geophysical Journal
793 International, 170(3), 995-1014.
794

795 Tiberi, C., Diament, M., Lyon Caen, H., & King, T. (2001). Moho topography beneath the
796 Corinth Rift area (Greece) from inversion of gravity data. Geophysical Journal
797 International, 145(3), 797-   808.
798

799 Uieda, L., Barbosa, V. C., & Braitenberg, C. (2016). tesseroids: Forward-modeling
800 gravitational fields in spherical coordinates. Geophysics, 81(5), F41-F48.
801

802 Vacher, P., Mocquet, A., & Sotin, C. (1998). Computation of seismic profiles from mineral
803 physics: the importance of the non-olivine components for explaining the 660 km depth
804 discontinuity. Physics of the Earth and Planetary Interiors, 106(3-4), 275-298.
805

806 Vrabec, M., & Fodor, L. (2006). Late Cenozoic tectonics of Slovenia: structural styles at the
807 Northeastern corner of the Adriatic microplate. In The Adria microplate: GPS geodesy,
808 tectonics and hazards (pp. 151-168). Springer, Dordrecht.
809

810 Wang, Y., He, Y., Lu, G., & Wen, L. (2020). Seismic, thermal and compositional structures of
811 the stagnant slab in the mantle transition zone beneath southeastern China. Tectonophysics,
812 775, 228208.
813

814 Webb, S. J. (2009). The use of potential field and seismological data to analyze the structure of
815 thelithosphere beneath southern Africa (Doctoral dissertation).
816

817 Wessel, P., Smith, W. H., Scharroo, R., Luis, J., & Wobbe, F. (2013). Generic mapping tools:
818 improved version released. Eos, Transactions American Geophysical Union, 94(45), 409-410.
819

820 Wessel, P., & Luis, J. F. (2017). The GMT/MATLAB Toolbox. Geochemistry, Geophysics,
821 Geosystems, 18(2), 811-823.
822

823 Workman, R. K., & Hart, S. R. (2005). Major and trace element composition of the depleted
824 MORB mantle (DMM). Earth and Planetary Science Letters, 231(1-2), 53-72.
825
826 Zeyen, H., & Fernàndez, M. (1994). Integrated lithospheric modeling combining thermal,
827 gravity, and local isostasy analysis: Application to the NE Spanish Geotransect. Journal of
828 Geophysical Research: Solid Earth, 99(B9), 18089-18102.
829
830 Zhao, L., Paul, A., Malusà, M. G., Xu, X., Zheng, T., Solarino, S., ... & Aubert, C. (2016).
831 Continuity of the Alpine slab unraveled by high-resolution P wave tomography. Journal of
832 Geophysical Research: Solid Earth, 121(12), 8720-8737.
833
834 Zingerle, P., Pail, R., Gruber, T., & Oikonomidou, X. (2020). The combined global gravity field
835 model XGM2019e. *Journal of Geodesy*, *94*(7), 1-12.
836

837 **Appendix A Gravity Gradients at satellite height**

838 For all Alpine density models presented above (section 3, 4,1 and 4.2) we have also calculated

839 gravity gradients at a station height of 225 km. This station height corresponds to the second

840 mission phase of GOCE (Gravity field and steady-state ocean circulation explorer) carried out

841 by ESA (European Space Agency).

842 We anticipated that gravity gradients measured by the GOCE satellite mission are sensitive to

843 the slab segments in the Alpine region. Our result show, that the long wavelength signal of the

844 different present slab segments contributes to a large-scale gravity response where the different

845 contributor cannot be separated. Therefore, we conclude that against our anticipation gravity

846 gradients at satellite height are in fact not sensitive to the Alpine slab configuration. We show

847 here, the gravity gradients (mainly the gzz component) for completeness.

848 Measured gravity gradients from the GOCE mission (Bouman et al., 2016), which were

849 corrected for topography and bathymetry ranges from 2.5 to -2.5 E at satellite altitude of 225

850 km height (Fig. 13). A negative gravity anomaly of -2.5 E in the gzz component is observed

851 equivalent to the vertical gz component (Fig. 13). However, no clear sign for subducting

852 lithosphere can be observed in any component of the gravity gradient tensor.
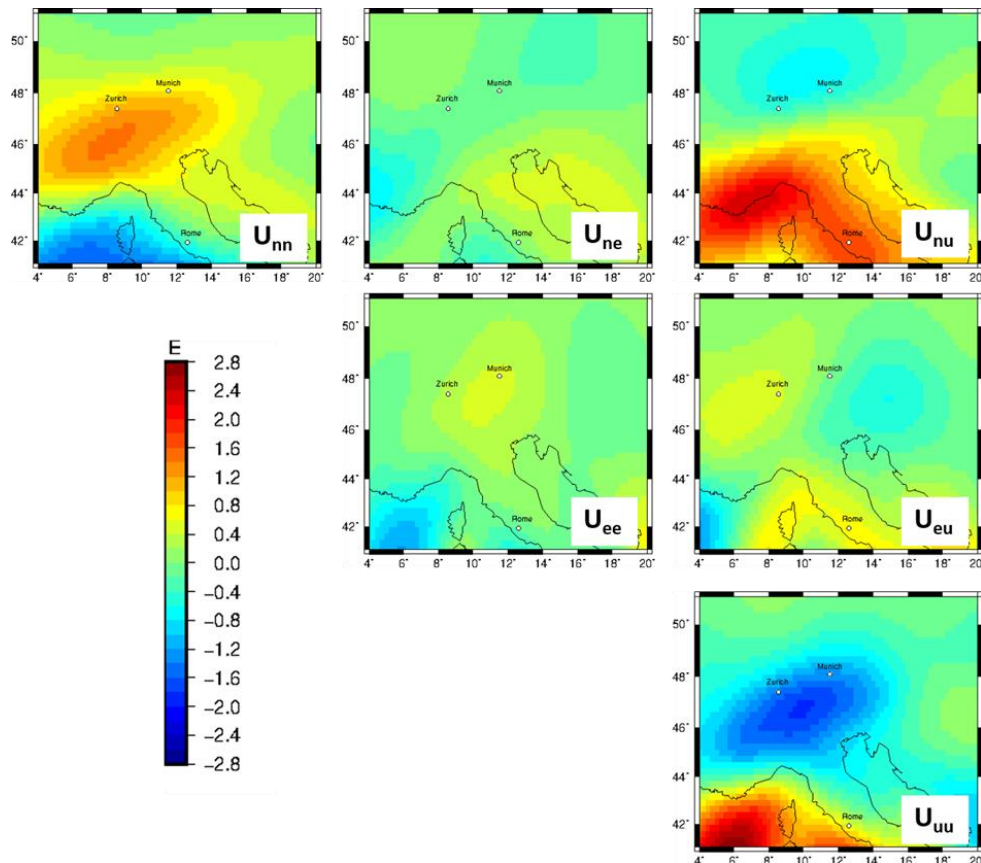
853
854 *Figure 13 GOCE gradients at 225 km height after Bouman et al. (2016) corrected for topography and bathymetry with a 5°*
855 *extension to remove far filed effects. The gravity gradients are presented in a North-East-Up coordinate system.*

856 The forward calculated gzz component at 225 km station height from a density model (section

857 3) with converted densities ranges from -3.5 E to 0.7 E (Fig. 14). A positive gravity signal of

858 about 0.5 E in the Apennine and Alpine region is observed which could be linked to subducting

859 slab segments. However, it is impossible to separate specific slab segments.
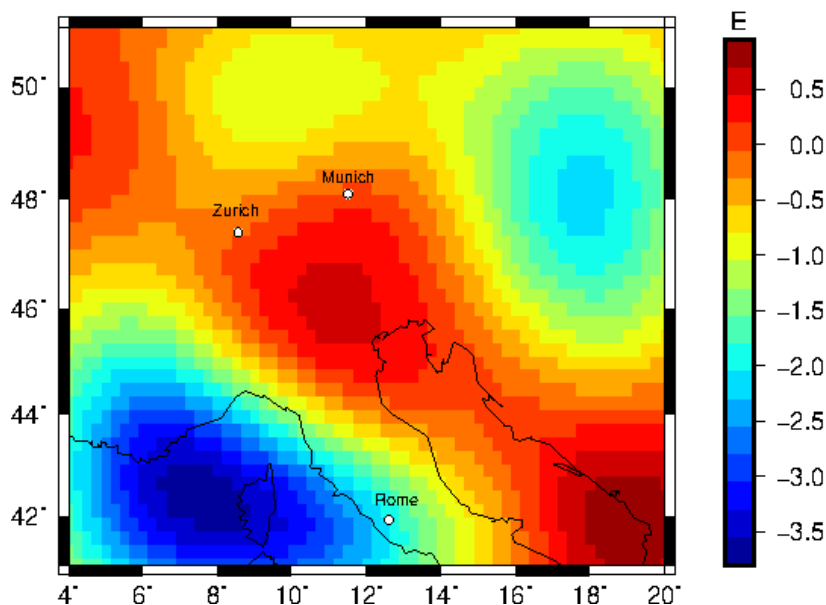
860
861 *Figure 14 Forward calculated gzz gravity signal from relative density distribution converted from relative seismic velocities*
862 *using a conversion factor of 0.3.for the at 225 km station height.*

863 Forward calculated tesseroid models (section 4.1) for slab configuration 1 and 2 with a constant

864 density contrast of 60 kg/m^3 and a constant thickness of 80 km result in a less sharp gravity

865 signal for the gzz component at a station height of 225 km (Fig. 15) compared to the gz

866 component at station height of 6040 m (Fig. 6). The gravity signal for the gzz component is in

867 the range of 0.8 E to 1 E. At satellite altitude the gravity signal is observed as a large area with

868 a positive gravity effect for Configuration 1 and 2. The contribution of the different slab

869 segments to this positive gravity effect is not distinguishable. The only recognizable difference

870 is the size of this positive gravity signal. Configuration 1 shows a smaller anomaly, due to a

871 lower volume of subducting material in the Eastern Alps.
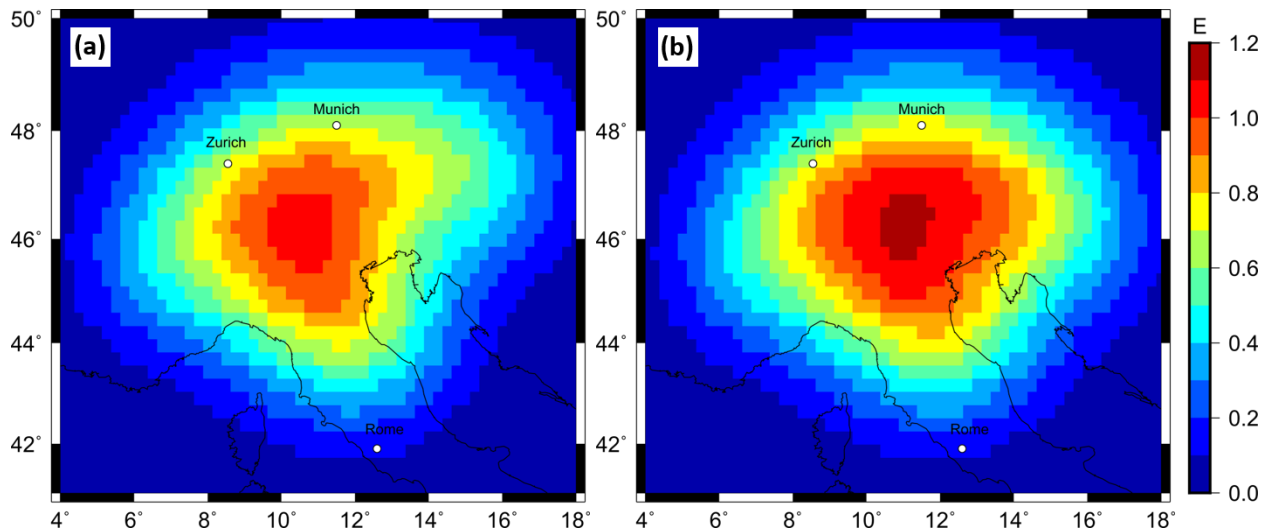
872

873 *Figure 15 Forward calculated gzz gravity signal at a station height of 225 km from predefined sub-crustal slab geometries with*
874 *a content density contrast of 60 kg/ m^3 and a constant thickness of 80 km. **(a)** slab configuration of hypothesis 1 **(b)** slab*
875 *configuration of hypothesis 2.*

876 In Addition, the signal strength for the forward calculated gzz component show the same

877 dependency of signal strength to the density contrast and slab thickness (Fig. 16) as the gz

878 component (Fig. 7). The signal strength of the gzz component ranges for the 12 different

879 combinations from 0.3 E to 2 E (Fig. 16). The gravity signal cannot be separated and affiliated

880 to a certain slab segment. The gzz gradient signal shows a large blurry gravity high over the

881 Alps, which thins out to the edges.
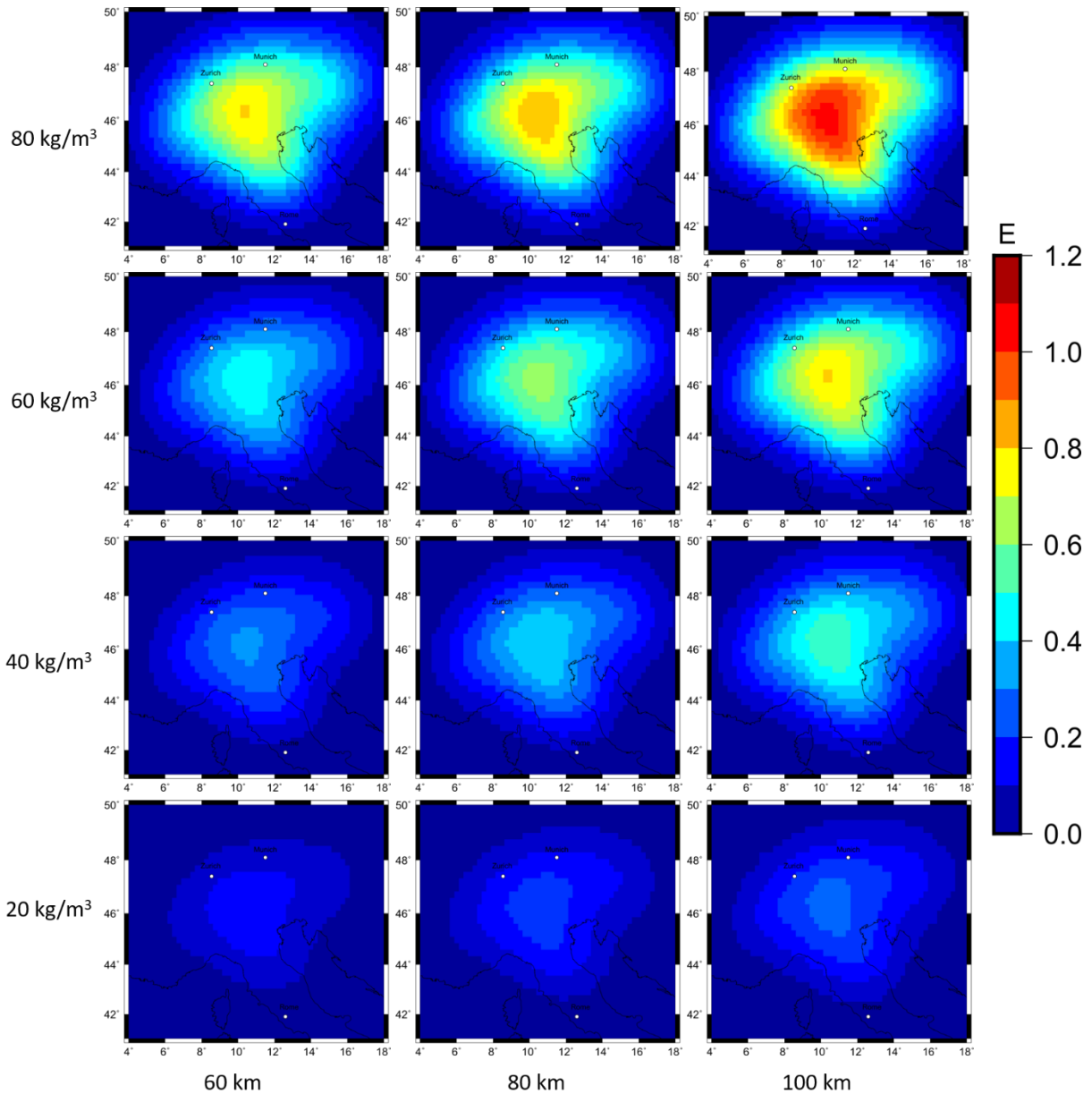
882
883 *Figure 16 Forward calculated gzz gravity signal for 12 different combination of density contrast and slab thickness at a station*
884 *height of 225 km for sub-crustal slab configuration 1.*

885 The gravity effect for the LitMod models (section 4.2) with the slab Configuration 1 shows in

886 the lithosphere domain a signal strength of about 0.05 E, while the sub lithospheric gravity

887 signal is in the range of 0.1 E for the gzz component at satellite altitude of 225 km height. The

888 combined gravity signal is in the order of 0.14 E (Fig. 17). A Proterozoic slab produces a larger

889 amplitude in signal strength, however the different slab segments can again not be separated

890 (Fig. 18).
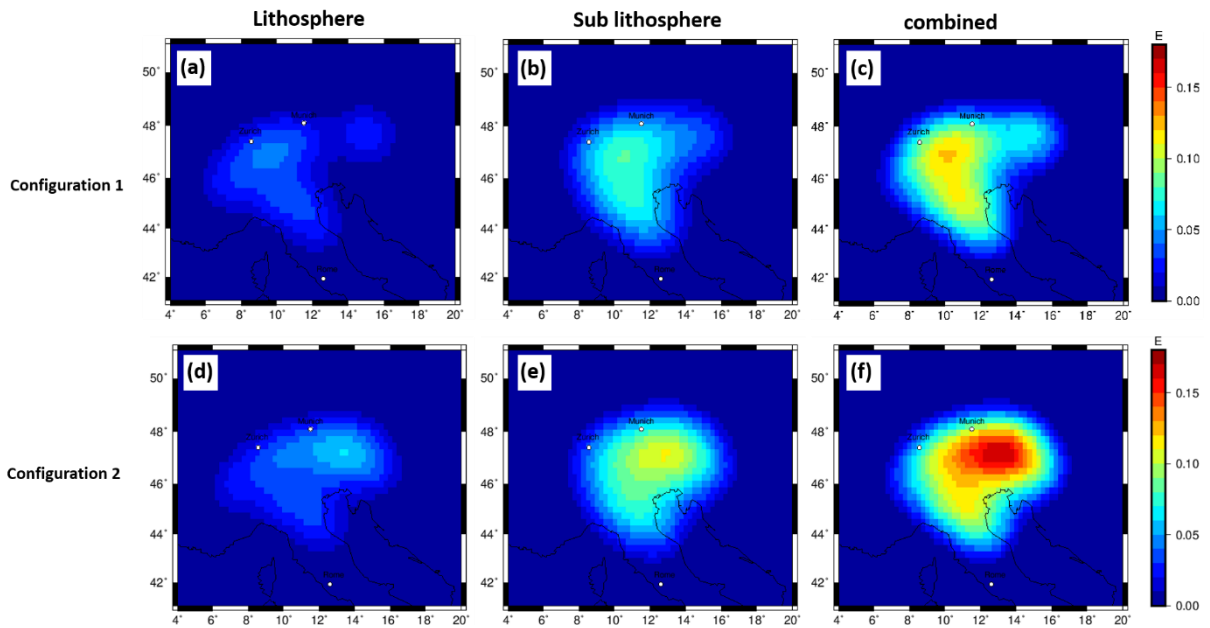
891
892 *Figure 17 forward calculated gzz gravity signal at satellite altitude of 225 km based on LitMod models with tecton like*
893 *compositions in the lithosphere and PUM and DMM compositions in the sub lithosphere (M_1, M_2, M_3, M_4) with an additional*
894 *thermal anomaly of -100° K for the sub-lithospheric slab segment, for predefined slab Configuration to the background model*
895 *M_0.* **(a)-(c)** *for Configuration 1.* **(d)-(f)** *for Configuration 2. Topographic and crustal effects are nullified.*
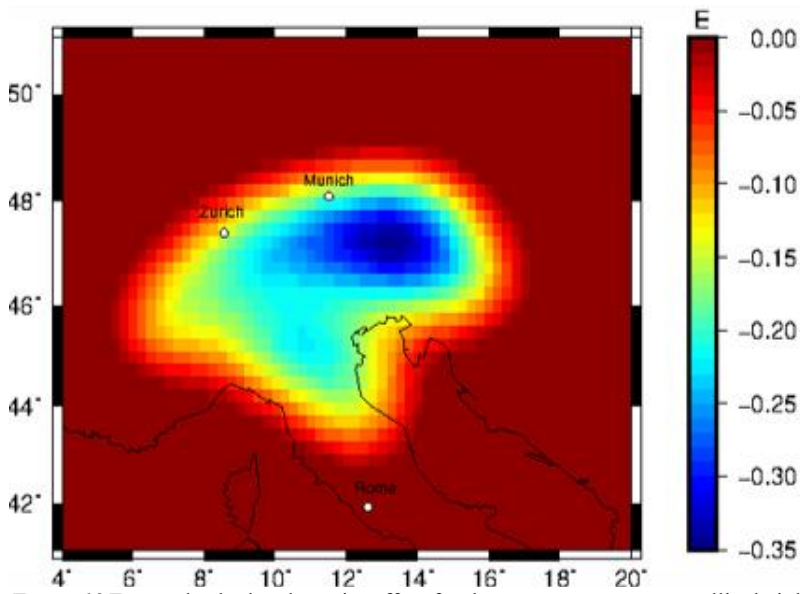
896
897 *Figure 18* Forward calculated gravity effect for the gzz component at satellite height of a Proterozoic lithospheric slab segment
898 to a Tecton compositional surrounding mantle for Configuration 2 obtained by calculating the residual between M_8 and M_0.

899